Geochemistry Geophysics Geosystems G3
AN ELECTRONIC JOURNAL OF THE EARTH SCIENCES
Published by AGU and the Geochemical Society

Article
Volume 6, Number 1
22 January 2005
Q01006, doi:10.1029/2004GC000714
ISSN: 1525-2027

Morphological and geochemical variations along the eastern Galápagos Spreading Center

David M. Christie
Department of Oceanographic and Atmospheric Sciences, Oregon State University, 104 Oceanic Administration Building, Corvallis, Oregon 97331-5503, USA (dchristie@coas.oregonstate.edu)

Reinhard Werner
Tethys Geoconsulting GmbH, Wischhofstraße 1-3, 24148 Kiel, Germany (rwerner@ifm-geomar.de)

Folkmar Hauff and Kaj Hoernle
Leibniz Institute for Marine Sciences (IFM-GEOMAR), Wischhofstraße 1-3, 24148 Kiel, Germany (fhauff@ifm-geomar.de; khoernle@ifm-geomar.de)

Barry B. Hanan
Department of Geological Sciences, San Diego State University, 5500 Campanile Drive, San Diego, California 92182-1020, USA (barry.hanan@sdsu.edu)

[1] As the eastern Galápagos Spreading Center (GSC) shallows westward toward the Galápagos Archipelago, axial morphology evolves from a low-relief, valley-and-ridge terrain to an increasingly prominent axial ridge, closely mirroring the western GSC. Between the Inca Transform (~85.5°W) and its western termination near 91°W, the eastern GSC comprises seven morphological segments, separated by five morphological discontinuities and the eastward propagating 87°W overlapping spreading center. Combined morphologic and geochemical data divide the eastern GSC into two domains independent of the fine-scale morphologic segmentation. The western domain is defined by its axial ridge morphology and highly variable lava population. Elemental data define steep along-axis gradients, reflecting a complex source that includes one or more hot spot–related components in addition to a highly depleted component. The eastern domain is defined by transitional, valley-and-ridge morphologies and a surprisingly invariant lava population. This population is dominated by shallow crystal fractionation processes and displays significantly less variability attributable to multiple source components. The Galápagos hot spot has long been known to have a symmetrical, long-wavelength influence on crustal accretion along the GSC. Existing isotopic and new elemental data define twin "geochemical peaks" that we interpret as loci for transfer of distinct source components from the Galápagos plume to the GSC. Although Na_8 and Fe_8 values lie within the negatively correlated global array, Na_8 increases with decreasing axial depth, contrary to global trends and consistent with emerging deep, hydrous melting models that predict decreasing overall extent of melting despite increasing melt production. Support for hydrous melting comes from decreasing heavy REE, increasing La/Sm and La/Yb, and the systematics of decreasing FeO and increasing CaO and Al_2O_3 with decreasing distance to the hot spot. Overall, an enriched, deep melt component appears to coexist in the shallow mantle with a ubiquitous, depleted primitive melt component, consistent with new models for channelized melt flow connecting a deep hydrous melt regime with the dry shallow mantle. Nevertheless, an absence of low-Fe lavas suggests that hydrous melting is strictly limited beneath the eastern GSC, becoming dominant only near the western geochemical peak where input from a hydrous "Northern" or "Wolf-Darwin" plume component is inferred.

Components: 18,991 words, 20 figures, 4 tables.

Keywords: Galapagos Spreading Center; ridge-hot spot interaction; axial morphology; mid-ocean ridge geochemistry; intermediate spreading rate; morphologic transitions.

Index Terms: 3035 Marine Geology and Geophysics: Midocean ridge processes; 3045 Marine Geology and Geophysics: Seafloor morphology, geology, and geophysics.

Received 6 February 2004; **Revised** 18 October 2004; **Accepted** 4 November 2004; **Published** 22 January 2005.

Christie, D. M., R. Werner, F. Hauff, K. Hoernle, and B. B. Hanan (2005), Morphological and geochemical variations along the eastern Galápagos Spreading Center, *Geochem. Geophys. Geosyst.*, *6*, Q01006, doi:10.1029/2004GC000714.

1. Introduction

[2] Strong gradients in mid-ocean ridge axial depth and basalt geochemistry induced by nearby oceanic hot spots are well known on regional scales of several hundred kilometers [e.g., *Schilling et al.*, 1982; *Schilling*, 1991], but segment-scale (tens of kilometers) variations in segmentation, morphology, magmatism and, especially, geochemical variability are not yet well known. However, recent data from the western Galápagos Spreading Center (GSC) [*Detrick et al.*, 2002, *Sinton et al.*, 2003] and from the eastern GSC, presented here, suggest that segment-scale variability, in addition to carrying fundamental information about the thermal and chemical structure of the spreading center itself, can also help to define patterns of melting and mantle flow associated with plume-ridge interaction.

[3] The region within which the GSC passes close to the Galápagos Archipelago is uniquely suited for studies of the mantle dynamics underlying hot spot-spreading–center interaction and, potentially of mantle plume structure, because of the unique plate motions in this area. During the last ~5 m.y., rapid migration of the GSC to the northeast, away from the Galápagos hot spot, has progressively separated the locus of spreading from the plume source [e.g., *Hey*, 1977; *Wilson and Hey*, 1995; *Ito et al.*, 1997; *Sallarès and Charvis*, 2003]. This dynamic separation is inferred to deflect and disperse plume flow beneath the lithosphere, allowing the internal structure of the plume to be inferred from areal patterns of lava geochemistry across the Galápagos platform and along the GSC [*White and Hofmann*, 1978; *White*, 1979; *Geist et al.*, 1988; *Geist*, 1992; *White et al.*, 1993; *Graham et al.*, 1993; *Sinton et al.*, 1996, 1997; *Kurz and Geist*, 1999; *Harpp and White*, 2001; *Blichert-Toft and White*, 2001; *Harpp et al.*, 2002].

[4] During R/V *Sonne* Cruise SO 158 (MEGAPRINT) we conducted continuous multibeam mapping and systematic dredge sampling primarily along the eastern GSC between the Inca Transform (~85.5°W) and the 91°W transform with sparse sampling of the western GSC between the 91°W transform and ~92.5°W where the line of the Wolf-Darwin seamounts intersects the GSC (Figure 1; dredge locations shown in Figures 4–11). This paper presents new morphological and geochemical data from this cruise and complements a detailed study of the western GSC by *Detrick et al.* [2002], *Canales et al.* [2002], *Sinton et al.* [2003], and *Cushman et al.* [2004].

2. Regional Setting

[5] The mantle plume inferred beneath the Galápagos hot spot is a long-lived feature. The oldest lavas attributed to this plume include basalts up to 139 Ma from the Nicoya peninsula in Costa Rica [*Hoernle et al.*, 2004] and the ~93 Ma flood basalts of the Caribbean Plateau [*Duncan and Hargraves*, 1984; *Sinton et al.*, 1997; *Hauff et al.*, 1997, 2000a, 2000b; *Geldmacher et al.*, 2003]. More recently, the paired Cocos and Carnegie Ridges were constructed from ~20 to ~5 Ma on the Cocos and Nazca plates while the spreading axis was located above the Galápagos hot spot [e.g., *Hey*, 1977; *Lonsdale and Klitgord*, 1978; *Wilson and Hey*, 1995; *Werner et al.*, 2003]. But since ~5 Ma, the spreading center has migrated to the northeast, away from the hot spot, resulting in significant reduction of magma supply to, and volcanic construction at, the southern end of Cocos Ridge [*Hey et al.*, 1977; *Wilson and Hey*, 1995; *Ito and Lin*, 1995a, 1995b]. At the same time, the supply of material to the Nazca plate appears to have increased, broadening Carnegie Ridge to form the shallow Galápagos Platform. During this same interval, northward migration of the GSC has led to the formation, by seafloor spreading, of a region of young, weak lithosphere between the GSC and the Galápagos Platform.

2.1. Galápagos Archipelago and Platform

[6] Coeval volcanism is widely dispersed across the Galápagos Platform, suggesting that the under-

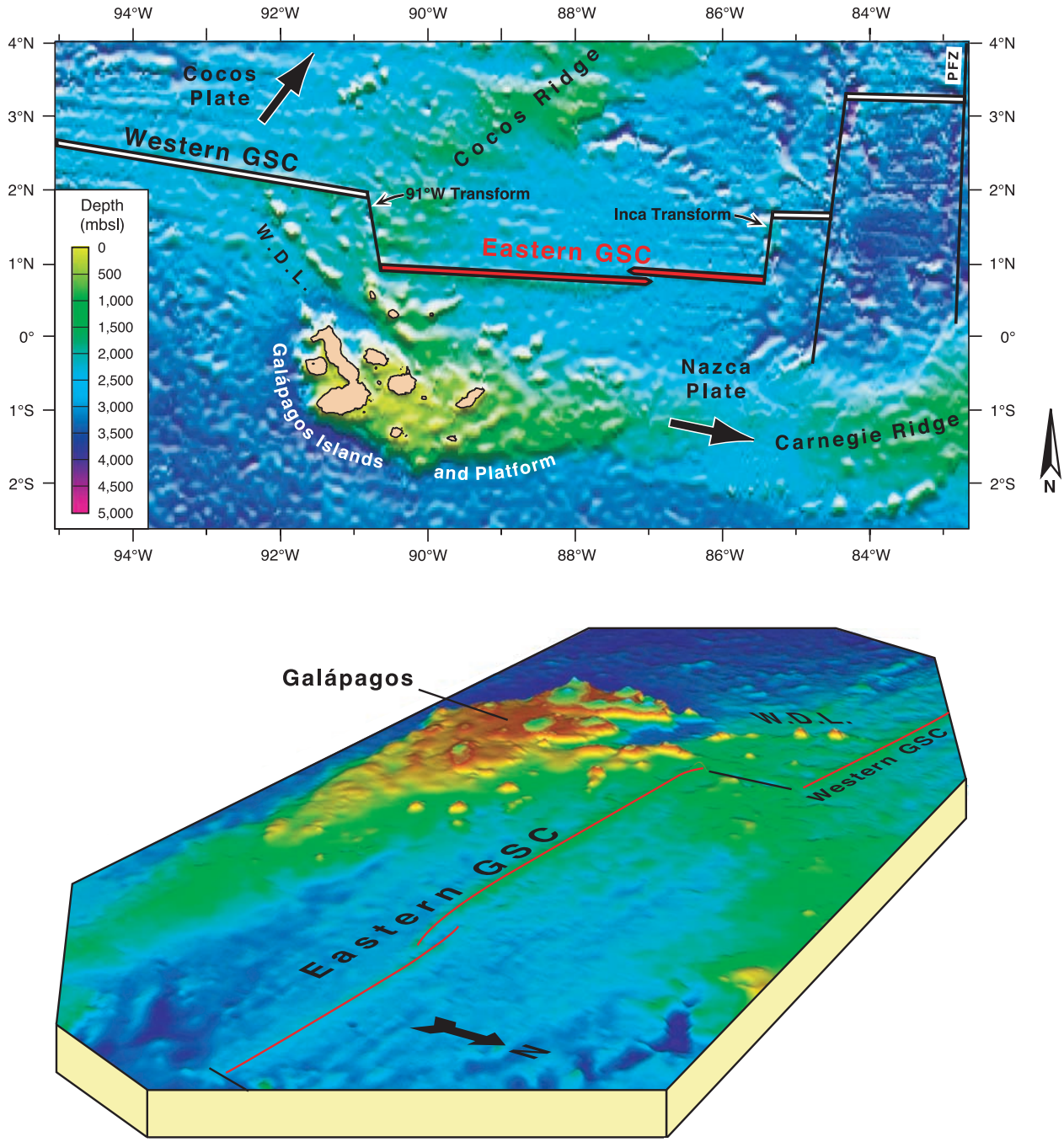

Figure 1. (a) Bathymetric map of the Galápagos area based on satellite-derived seafloor topography by *Smith and Sandwell* [1997]. The eastern Galápagos Spreading Center (GSC), bounded by the Inca Transform and the 91°W transform, is marked in red. Relative plate motion according to *Kellogg and Vega* [1995]. W.D.L., Wolf-Darwin-Lineament. (b) Three-dimensional picture showing the eastern GSC and the Galápagos Platform based on satellite-derived seafloor topography.

lying mantle plume is sheared and dispersed over a wide downstream area by the relatively rapid (>60 mm/yr) eastward motion of the Nazca plate [*White et al.*, 1993; *Harpp*, 1995; *Harpp and White*, 2001]. When the isotopic and trace element ratios from these widely dispersed volcanoes are relocated to their points of eruption (based on radiometric ages and known plate motion) and contoured, they describe a remarkable "horseshoe" pattern. More enriched lavas occur around the outer margins of the platform with more depleted lavas toward the center.

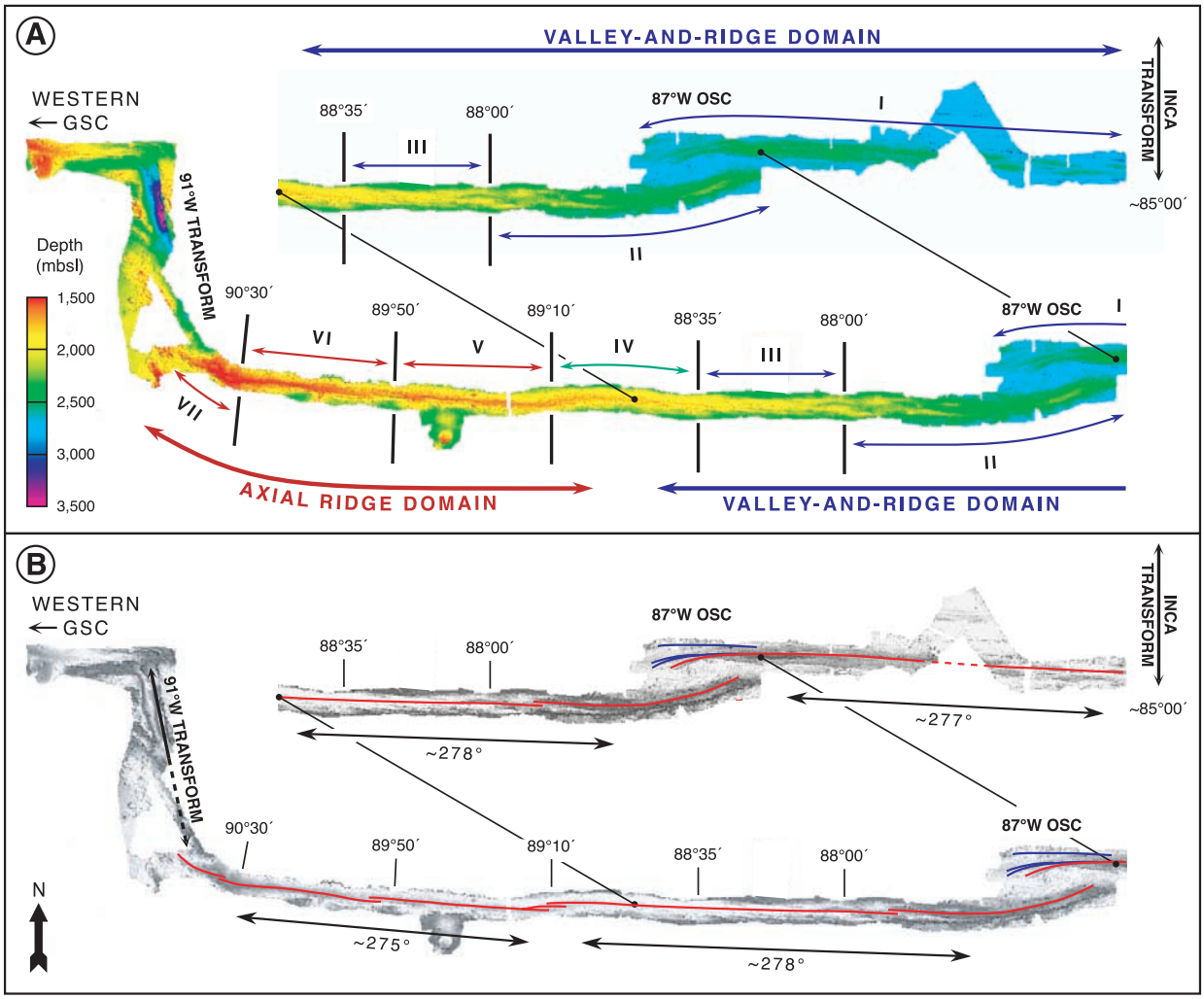

Figure 2. (a) Overview map illustrating the segmentation and morphological evolution of the eastern GSC. The easternmost three segments (I–III) constitute a valley-and-ridge morphologic and magmatic domain that evolves across a transitional Segment IV to an axial ridge domain (Segments V–VII). Bathymetry is based on SIMRAD EM 120 multibeam data from cruise SO 158 of R/V *Sonne*, merged with multibeam data of R/V *Ewing* cruise EW0004 [*Detrick et al.*, 2002; *Sinton et al.*, 2003]. (b) Shaded relief showing the current spreading axis (red line) and its average orientation. Blue lines indicate abandoned strands at the 87° OSC.

[7] The Galápagos mantle plume is also inferred to be internally heterogeneous. Pb and Sr isotopic ratios are highest (for a given εNd) in lavas from the southern margin, and at least four distinct mantle components are required to account for the multidimensional array of Sr, Nd, Pb, Hf, and He isotopic ratios in Galápagos Platform lavas [*White et al.*, 1993; *Harpp*, 1995; *Harpp and White*, 2001; *Blichert-Toft and White*, 2001; *Hoernle et al.*, 2000]. Of these, the three more enriched mantle components have been interpreted as derived from a heterogeneous plume. A fourth, depleted component has been attributed to ambient, depleted (MORB source) upper mantle [*White et al.*, 1993], or to a fourth plume component derived from material that is progressively depleted by continuous melt extraction during flow toward the spreading center [*Hoernle et al.*, 2000]. Each of the three plume-components is most strongly expressed in a distinct geographic province and they have become known by geographic names. *Harpp and White* [2001] defined Floreana, Wolf-Darwin, and Plume components, while *Hoernle et al.* [2000], *Geldmacher et al.* [2003], and *Werner et al.* [2003] defined northern, central, and southern components that are also identifiable in Galápagos hot spot track lavas up to ~20 Ma from Cocos, Carnegie, Malpelo, and Coiba Ridges, suggesting that these are persistent components of the Galápagos mantle plume.

Table 1. Eastern Galápagos Spreading Center Segments

Segment	Longitude, W		Length, km	Boundary	Axial Depth, mbsl	Main Morphological Features
	Start	End				
				Inca Transform		
Valley-and-Ridge Domain						
Segment I	~85°00′	87°30′	~270		2,800–2,500	multiple overlapping parallel valleys; axial ridge with parallel summit grabens
				87° OSC		
Segment II	87°00′	88°00′	~110		2,500–1,950	distinct valley bounded by narrow ridges; ~4 km offset at 87°52′W
				transition into a broad ridge		
Segment III	88°00′	88°35′	~65		1,950–1,850	low-amplitude valley-and-ridge topography on top of a broad ridge
				pronounced valley and ridge topography passes into an axial high		
Transitional Domain						
Segment IV	88°35′	89°10′	~65		1,850–1,750	subdued axial ridge with a continuous narrow axial summit trough
				~3 km en echelon offset		
Axial Ridge Domain						
Segment V	89°10′	89°50′	~75		1,680 ± 25	axial ridge with continuous narrow crest, no axial graben
				narrow crest passes into low-amplitude valley-and-ridge terrain		
Segment VI	89°50′	90°30′	~75		1,680–1,500	two subsegments (valley-and-ridge terrain and distinct crest) on top of an axial ridge; ~3 km offset at ~90°W
				transition into a broad, voluminous ridge		
Segment VII	90°30′	90°45′	~30		1,500–1,490–~1,900	most voluminous axial ridge at the E-GSC, two overlapping volcanic shields with calderas, ~2 km offset at ~90°34′W
				±91°W transform (Segment VII appears to extend some km beyond the transform)		

2.2. Galápagos Spreading Center

[8] Over a distance of ~600 km on either side of the 91°W transform, the Galápagos Spreading Center shoals by ~1 km, mantle Bouguer anomaly amplitude decreases by ~90 mGal, and axial valley morphology transitions to an axial ridge, as mantle temperature and magma supply rate increase toward the shallowest part of the GSC [e.g., *Christie and Sinton*, 1981; *Schilling et al.*, 1982; *Ito and Lin*, 1995a; *Canales et al.*, 1997, 2002; *Detrick et al.*, 2002; *Sinton et al.*, 2003].

[9] The morphology of the western GSC has recently been documented in detail by *Sinton et al.* [2003], who recognized three morphological provinces. The western province, west of 95°30′W, strikes ~092° and is characterized by an axial valley morphology and by mostly small left-stepping non-transform offsets. The middle province, between the 95°30′W and 93°15′W propagating rift tips strikes ~096° and is characterized by transitional axial morphology with similar left-stepping offsets to those of the western province. The eastern province strikes ~100° and is characterized by axial ridge morphology with predominantly right-stepping non-transform offsets. Thus there appears to be a progressive, west-to-east, clockwise rotation of the axis toward the hot spot. Together with the switch from left- to right-stepping offsets approaching the 91°W transform, this rotation suggests that, with increasing proximity to the hot spot, there is an increasing tendency for the locus of spreading to lag behind the overall northeastward (absolute) migration of the GSC.

[10] Several geochemical tracers, including $^{87}Sr/^{86}Sr$, La/Sm, K_2O, and K/Ti increase monotonically ($^{143}Nd/^{144}Nd$ and $^{176}Hf/^{177}Hf$ decrease), reaching along-axis maxima (or minima) within the axial depth minimum close to the hot spot, between 90°–92°W. These observations have been interpreted as reflecting a systematically increasing thermal and material contribution from the Galápagos mantle plume to axial topography and to GSC lava compositions [e.g., *Schilling et al.*, 1982, 2003; *Verma and Schilling*, 1982; *Verma et al.*, 1983; *Ito and Lin*, 1995a; *Schilling*, 1991; *Canales et al.*, 1997]. Viewed on a regional scale, the morphological, geophysical, and geochemical maxima (and minima) appear to coincide within reasonable limits. At segment-scale, however, peak locations for individual geochemical tracers commonly differ from one another or from those for other parameters by ~100 km (see detailed discussion in section 5.1). *Verma et al.* [1983] suggested that apparent shifts in geochemical peaks reflect variations in degree of melting and melt segregation depth.

3. Morphological Variations Along the Eastern GSC

3.1. Overall Morphology

[11] Over its 600-km length, from the Inca Transform near 85°W to its closest approach to the Galápagos Archipelago near 91°W, the strike of the eastern GSC remains almost constant at ~277° (Figure 2), comparable to the middle province of the western GSC. The eastern GSC is divided into seven morphological segments separated by five morphological discontinuities and the 87°W overlapping spreading center (OSC) [*Perram and Macdonald*, 1994] (Figure 2a). Off-axis magnetic anomaly patterns indicate that the 87°W OSC is the present tip of a ridge segment that has propagated rapidly eastward at ~120 mm/yr for the last ~2 m.y. [*Hey*, 1977; *Wilson and Hey*, 1995], but it is not known whether the overlapping morphology has been present throughout this time. The 87°W OSC and three of the four medium-scale (2–6 km) non-transform offsets along the eastern GSC are left-stepping. A single right-stepping offset occurs at ~90°34′W between the two volcanic shields of Segment VII. The predominance of left-stepping offsets mirrors the predominantly right stepping offsets of the eastern province of the western GSC [*Sinton et al.*, 2003] and could be interpreted as reflecting a similar tendency for the locus of spreading to locate as close as possible to the hot spot. However, the change in offset sense from the eastern to the middle province of the western GSC, and the accompanying strike rotation, are not mirrored along the eastern GSC. Rather, left-stepping offsets appear to reflect a dominant regional pattern that is perturbed by proximity to the hot spot only in the eastern province of the western GSC.

3.2. Segment-Scale Morphology

[12] Bathymetric mapping using the SIMRAD EM 120 multibeam echo sounder on R/V *Sonne* documents a systematic, east-west evolution from valley-and-ridge axial morphology (Segments I–III), through a transitional segment (IV), to increasingly broad axial ridges (Segments V–VII) (Figure 2a, Table 1). The term "valley-and-ridge" morphology used here corresponds to the previously used "transitional" morphology [*Canales et al.*, 1997, 2002; *Detrick et al.*, 2002; *Sinton et al.*, 2003]. We prefer

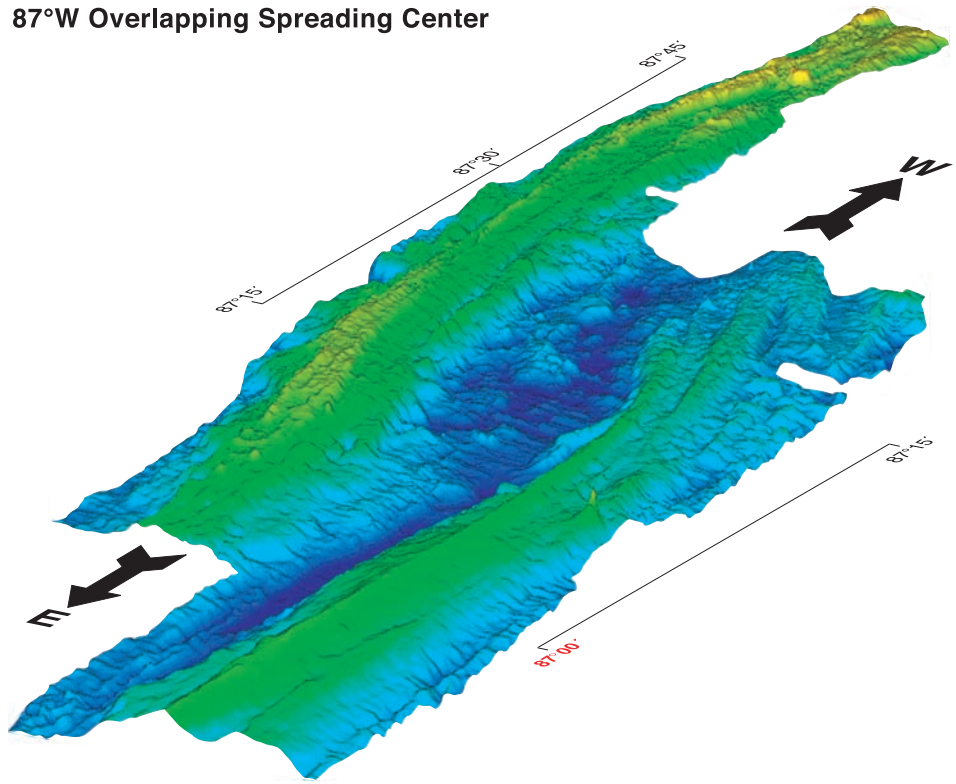

Figure 3. Oblique view of the 87°W overlapping spreading center from NE. Water depths range from >2,800 m (dark blue) to ~2,000 m (yellow). Note the multiple bifurcations of the northern (front) limb into several strands (see also Figure 4).

"valley-and-ridge" as a more descriptive term and because there are other transitional morphologies that occur at intermediate spreading rates. For example, *Shah and Sempéré* [1998] have documented along-axis transitions from axial ridges to axial valleys within individual transitional segments along the Southeast Indian Ridge. It should be emphasized that the widths and amplitudes (measured height from valley floor to flanking ridge crest) of these axial valleys-and-ridges are much smaller than those of the "axial ridge" and "axial valley" terrains typical of fast- and slow-spreading mid-ocean ridges, respectively. Within the valley-and-ridge terrains, it is often difficult to unequivocally identify the locus of spreading solely on the basis of morphology. In the following descriptions we identify as "axial" those ridges and valleys that appear to be most prominent and/or centrally located.

[13] The eastern GSC valley-and-ridge segments, Segments I–III, are characterized by multiple alternating valleys and ridges of relatively low amplitude (<500 m) that are continuous over tens of kilometers along strike. Segment I, the deepest, easternmost segment extends from the Inca Transform near 85°W to the 87°W OSC and is characterized by distinct valleys that are bounded by narrow ridges (Figure 4). Approaching its western tip (87°10′W–87°30′W), Segment I becomes the northern limb of the 87°W OSC and branches into three distinct, narrow strands. We interpret this bifurcation as resulting from transient, westward extension of the ridge by discrete volcano-tectonic events (Figures 3 and 4). These extensions are in the opposite direction from the long term eastward propagation of the 87°W OSC [*Hey*, 1977] and from the associated failure and eastward shortening of Segment I (see also section 4.1). Segment II extends from the 87°W OSC to 88°W. At its eastern end, a narrow axial ridge forms the southern limb of the 87°W OSC. Farther to the west a distinct valley becomes its dominant feature (Figure 5). Segment III (88°W–88°35′W) is characterized by a broad, 10-km-wide axial high, on top of which low-amplitude (>200 m) valley-and-ridge topography occurs (Figure 6). This pronounced valley-and-ridge topography largely disappears west of 88°27′W and passes into a subdued axial ridge (Segment IV; 88°35′ to 89°10′W) which represents the transition to the true axial ridge segments to the west (Figure 7).

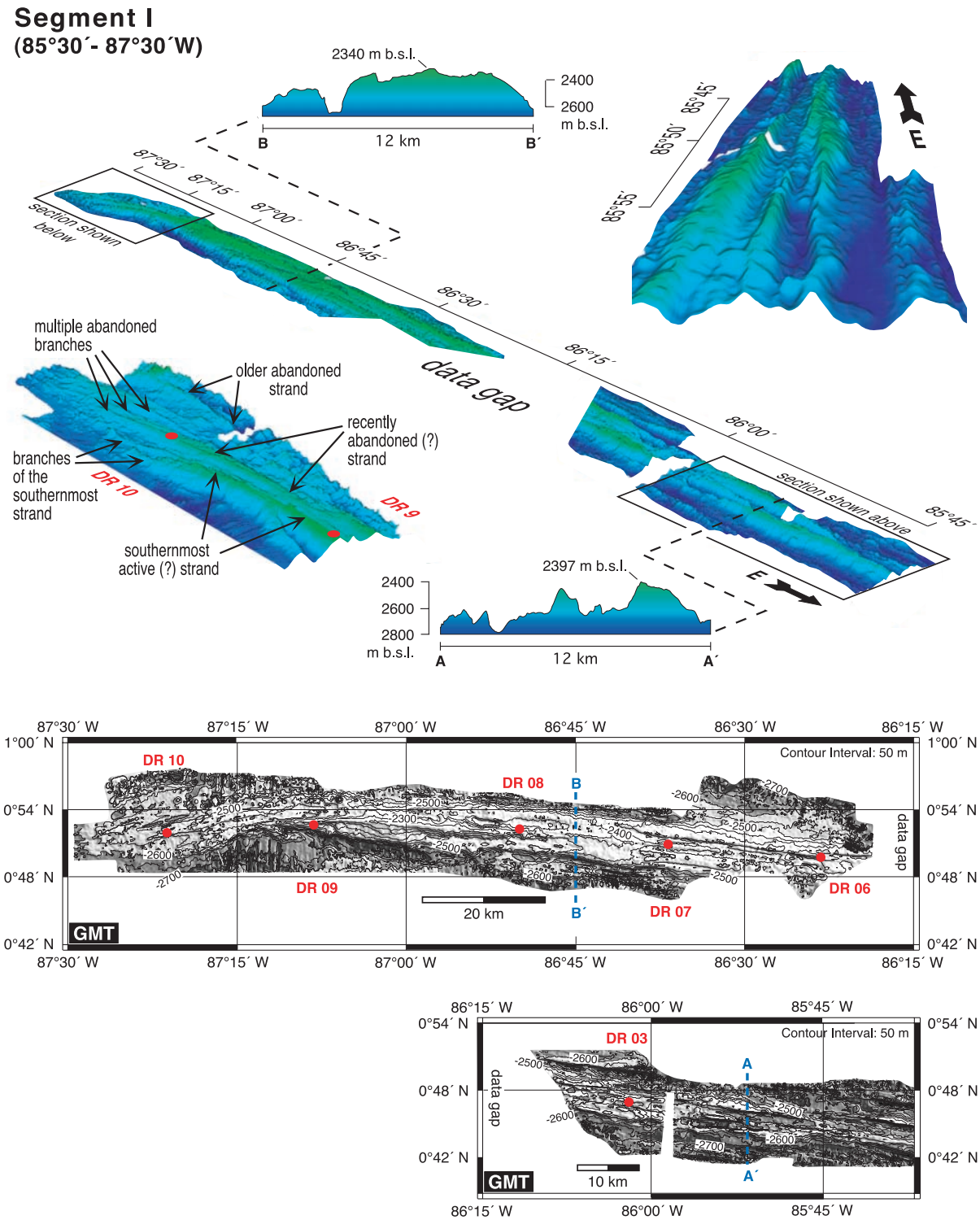
Segment I
(85°30´- 87°30´W)
2340 m b.s.l.
2400
2600
m b.s.l.
B
12 km
B´
87°30´
87°15´
87°00´
86°45´
86°30´
86°15´
86°00´
85°45´
85°45´
85°50´
85°55´
E
section shown below
data gap
section shown above
multiple abandoned branches
older abandoned strand
recently abandoned (?) strand
branches of the southernmost strand
DR 10
DR 9
southernmost active (?) strand
2397 m b.s.l.
2400
2600
2800
m b.s.l.
A
12 km
A´
87°30´ W
87°15´ W
87°00´ W
86°45´ W
86°30´ W
86°15´ W
1°00´ N
0°54´ N
0°48´ N
0°42´ N
Contour Interval: 50 m
DR 10
DR 08
DR 09
DR 07
DR 06
data gap
20 km
GMT
86°15´ W
86°00´ W
85°45´ W
DR 03
10 km

Figure 4

[14] The easternmost axial ridge Segment V (89°10′ to 89°50′W) is characterized by a relatively uniform axial ridge with a continuous narrow crest (Figure 8). Segment VI (89°50′–90°30′W) comprises two contrasting subsegments separated by a ~3 km left-lateral offset (Figure 9). The eastern subsegment consists of a broader axial high dissected by alternating ridges and grabens. We interpret this reversion to a valley-and-ridge terrain as the result of a transient local reduction in magma supply. The western subsegment forms a relatively steep axial ridge with a narrow crest. The westernmost Segment VII (90°30′W to 90°45′W) extends into, and most likely beyond, the southern end of the 91°W transform. At the closest point on the GSC to the Galápagos platform, the axial ridge is by far the most voluminous along the eastern GSC, broadening to form two small, en echelon shield volcanoes with summit calderas (Figure 10). These volcanoes are morphologically similar to, but smaller than, Axial Volcano on the Juan de Fuca Ridge [e.g., *Embley et al.*, 1990]. To the west of the shields the axial ridge abruptly decreases in volume. At ~90°41′W, it bends sharply northward to a strike of 312° and disappears at 90°45′W.

[15] Near 91°W, the axis of the GSC is offset by ~100 km. This offset is commonly referred to as the 91°W transform or Galápagos Transform [*Sinton et al.*, 2003], but existing incomplete bathymetric coverage suggests that the offset is accommodated within oblique, extensional basins lacking a well-defined transform fault trace. On the basis of magnetic data, *Wilson and Hey* [1995] suggested that the offset was initiated by a southward rift jump at ~3 Ma, most likely coinciding with the eastward propagation that has led to the present-day 87°W OSC. In contrast to all other major offsets of the GSC which have propagated away from the hot spot to the west or to the east, the location of the 91°W transform in the plate reference frame has remained essentially constant for the past ~2 m.y. [*Wilson and Hey*, 1995]. The northern part of the 91°W transform is a NNW–SSE trending, 3,500-m deep pull-apart basin (Figure 11). To the south, the basin narrows and shoals into a narrow, relatively shallow graben that trends SSE beyond the present map coverage. Because the available bathymetric maps are incomplete, the morphology of the southern part of the 91°W transform and its intersection with the complex morphology of Segment VII are unclear. It is clear, however, that the deep northern transform valley does not extend continuously to the eastern GSC and that Segment VII extends beyond the westernmost possible location of the southern intersection (Figure 11).

[16] In summary, the eastern GSC is dominated by the morphological transition from an eastern valley-and-ridge domain (Segment I–III) to a western axial ridge domain (Segments V–VI). The domain boundary is clearly defined between Segments III and IV, although the axial morphology evolves continuously on either side. A very similar transition occurs on the western GSC at approximately 92°35′W, on the basis of our interpretation of the maps of *Detrick et al.* [2002] and *Sinton et al.* [2003]. The transitions occur at very similar distances (~250 km) on either side of the 91°W transform, and at very similar axial depths (~1800 m). Both transitions correspond to minor axial discontinuities. In the valley-and-ridge domain of the eastern GSC,

Figure 4. Shaded relief images, maps, and cross sections of the valley-and-ridge-type Segment I (red points and numbers indicate SO 158 dredge sites). East of ~86°40′W multiple, up to ~4-km-wide and ~300-m-deep overlapping parallel valleys predominate, and the exact location of the axis of spreading cannot be recognized on the basis of morphology alone. Farther to the west (86°40′–87°10′W), a relatively broad, ~8-km-wide axial high is developed, on top of which several parallel summit grabens continue the more distinct valleys from farther east. Axial depths within the valleys of Segment I shoal from ~2,800 m in the east to ~2,500 m at the western end, while the bounding ridge crests shoal from 2,600 to 2,200 m. Approaching its western tip, Segment I becomes the northern limb of the 87°W OSC, turns slightly to the south, and, to the west of DR 9 (~87°08′W), branches into three distinct, narrow, terminal ridges surmounted by summit grabens (see also Figure 3). The southernmost strand, the most likely to be active, bifurcates at ~87°18′W into two >10-km-long branches. A similar pattern can also be seen on a recently abandoned strand that lies to the north and bifurcates into three or four small branches west of DR 10 (87°21′W). Still farther to the north, an older abandoned strand appears near ~87°10′W and extends to the west beyond the present map coverage. Because Segment I is failing as Segment II propagates to the east [*Hey*, 1977; *Wilson and Hey*, 1995], these multiple branching and partially overlapping strands suggest a pattern of west-propagating transient volcanic events, followed by eventual failure. The western terminus of Segment I is incrementally reestablished by formation of new branches that terminate progressively farther to the east. Assuming an eastward retreat of 120 mm/yr of the 87°W OSC [*Wilson and Hey*, 1995], these west-propagating events may happen every 50,000–100,000 years.

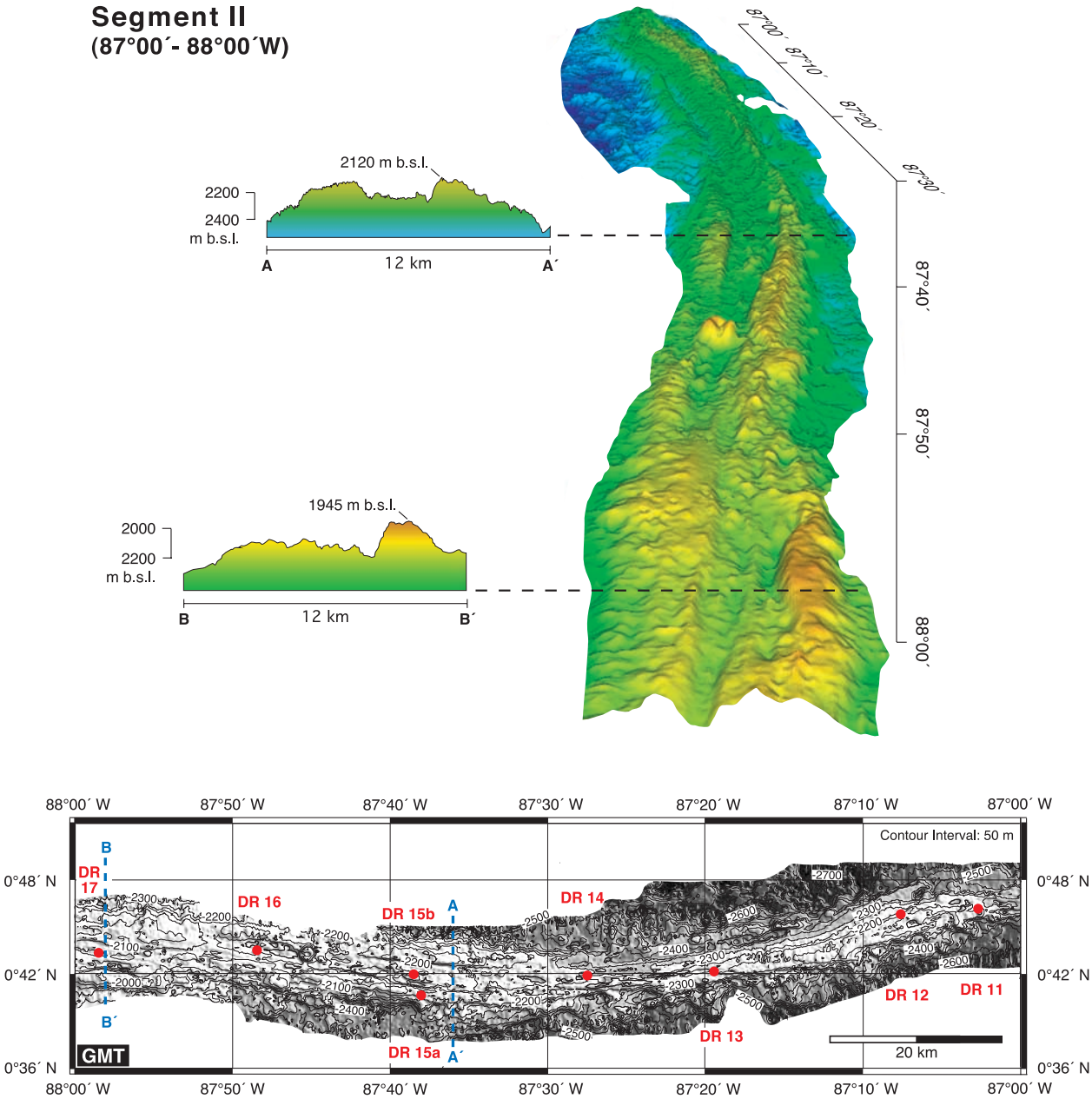

Figure 5. Valley-and-ridge-type Segment II. At its eastern end, a narrow axial ridge forms the southern, propagating limb of the 87°W OSC. Approaching the rift tip, this ridge curves to the north and deepens from ~2,200 m at ~87°15′W to ~2,500 m. West of 87°15′W, a distinct valley bounded by narrow, ~150- to 300-m-high ridges develops and shoals westward (from ~2,200 to ~1,950 meters below sea level (mbsl)) to become the probable locus of spreading. The width of the valley increases to more than 4 km and its depth increases to more than ~200 m at ~87°35′W. A ~200-m-high seamount located on the valley floor at 87°45′W appears to be split along an east-west line, suggesting that this axial volcano is astride the spreading axis. About 14 km farther west near ~87°52′W, the axial valley is offset ~4 km to the south. The formation of a broad ridge ~10 km west of this offset defines the eastern end of Segment III. Red points and numbers indicate SO 158 dredge sites.

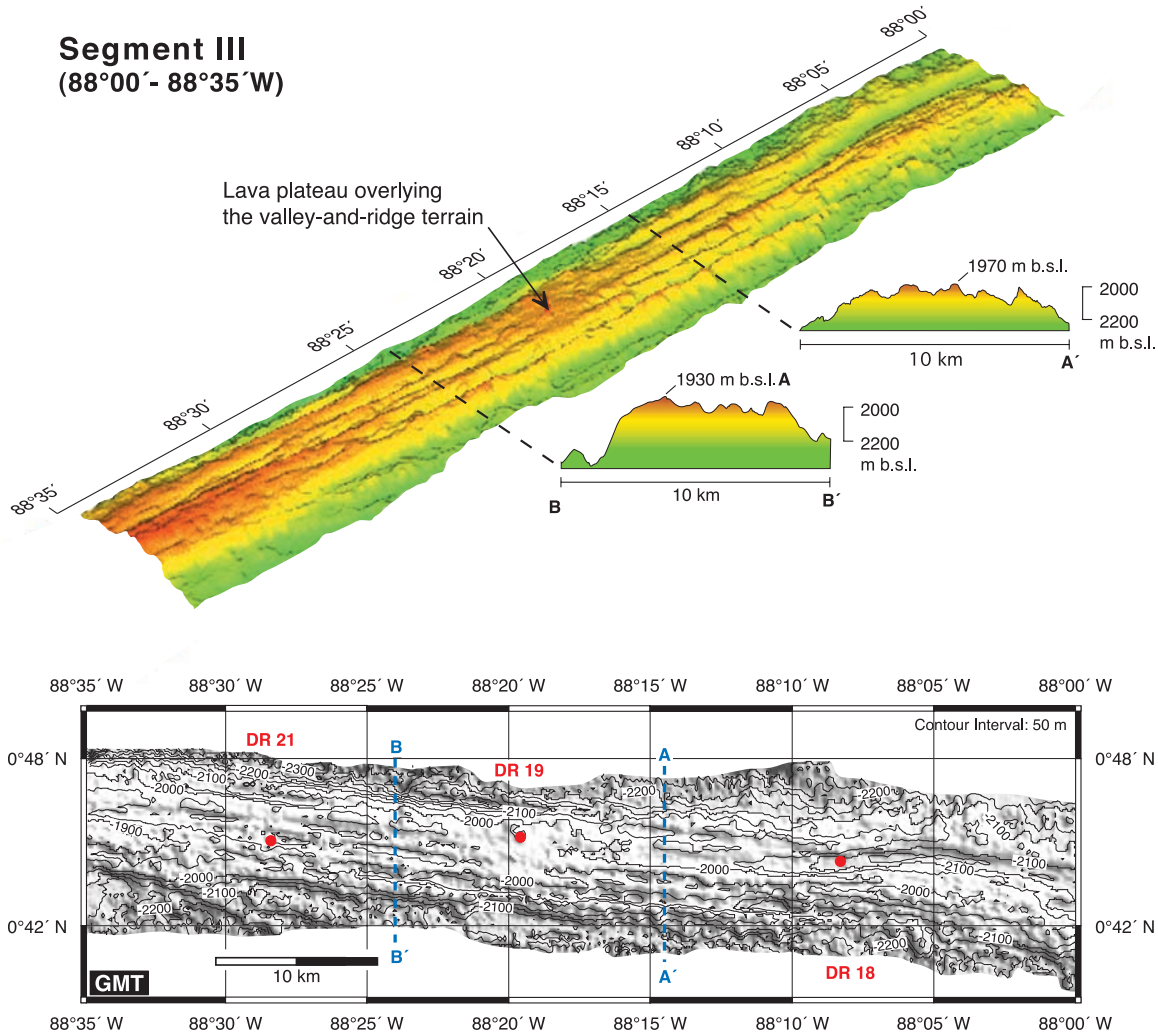

Figure 6. The axial region of the valley-and-ridge-type Segment III shoals slightly from ~2,000 m in the east to less than 1,900 mbsl at its western end. The axial rift valley characterizing Segment II seems to continue over the entire Segment III on the northern part of the ridge but narrows and shoals significantly in the westward direction. In the central part of Segment III (88°05′–88°27′W), up to five valleys less than 100 m deep and 2 km wide are situated on the top and flanks of the GSC, and the location of the axis is unclear. A recent high-volume eruption near ~88°20′W has created a lava plateau that obscures the underlying valley-and-ridge terrain. The disappearance of the pronounced valley-and-ridge topography west of 88°27′W marks the western boundary of Segment III. Red points and numbers indicate SO 158 dredge sites.

extrusion and tectonic extension are closely balanced. Prominent, axis-parallel faults, expressed by the episodic formation of small axial horst and graben structures, commonly occur close to the spreading axis and localized extrusive features are expressed as relatively broad ridges or lava shields. In the axial ridge domain, there is a continuous increase in height and volume of the GSC from ~89°W to a maximum in Segment VII (90°35′W). This morphologic evolution is generally consistent with increasing magma supply and increasing dominance of extrusive over tectonic processes. The high ridge volume in Segment VII may reflect a major influence of the Galápagos plume in this area, consistent with the results of recent isotope studies (T. F. Kokfelt et al., Plume-ridge interaction studied at the Galápagos Spreading Centre: Evidence from ^{226}Ra-^{230}Th-^{238}U and ^{231}Pa-^{235}U isotopic disequilibria, submitted to *Earth and Planetary Science Letters*, 2004; here-

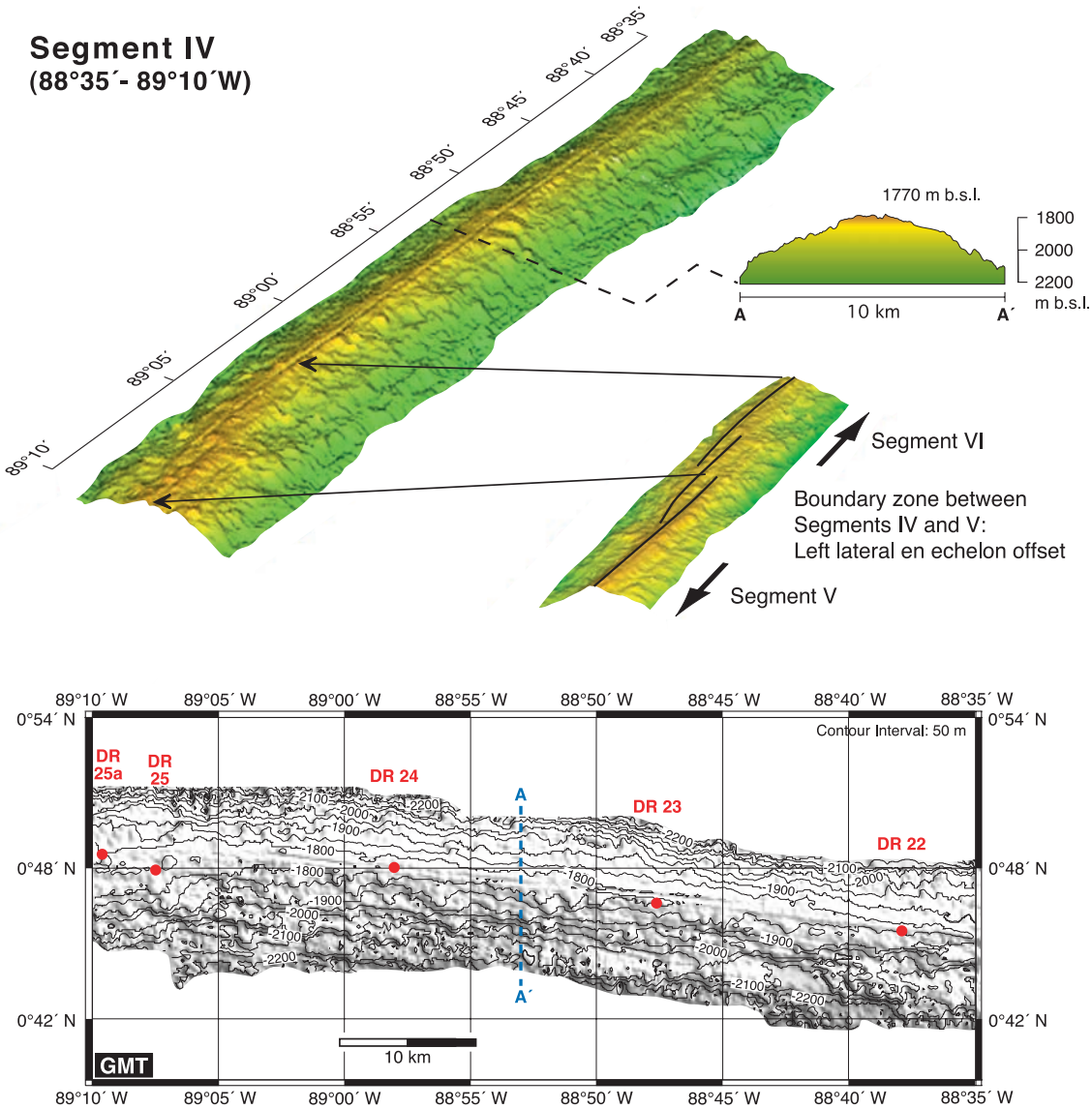

Figure 7. The transitional Segment IV is characterized by a subdued axial ridge with a continuous but narrow (100-m scale) and shallow (10-m scale) axial summit trough that is presumably the locus of volcanic activity. The axial ridge shoals to the west from 1,850 to 1,750 mbsl, and its cross-sectional area increases. Between Segments IV and V, an approximately 6-km-long left-lateral en echelon offset of the axial ridge and summit trough extends from ~89°05′ to 89°10′W, perhaps forming an incipient overlapping spreading center. Red points and numbers indicate SO 158 dredge sites.

inafter referred to as Kokfelt et al., submitted manuscript, 2004) (F. Hauff et al., personal communication, 2004). In addition, while axial depth decreases by 1,100 m along-axis (from ~2,600 mbsl at 86°W, to 1,500 mbsl near 91°W), average depth 8–12 km off-axis decreases by only 600 m (from ~2,700 to ~2,1000 mbsl [*Canales et al.*, 1997]). This suggests that excess axial topography is supported by thermal expansion of the hotter lithosphere close to the hot spot [*Canales et al.*, 2002; *Detrick et al.*, 2002].

4. Geochemical Variations Along the Eastern GSC

[17] Geochemical gradients have long been recognized along the GSC and attributed to thermal and

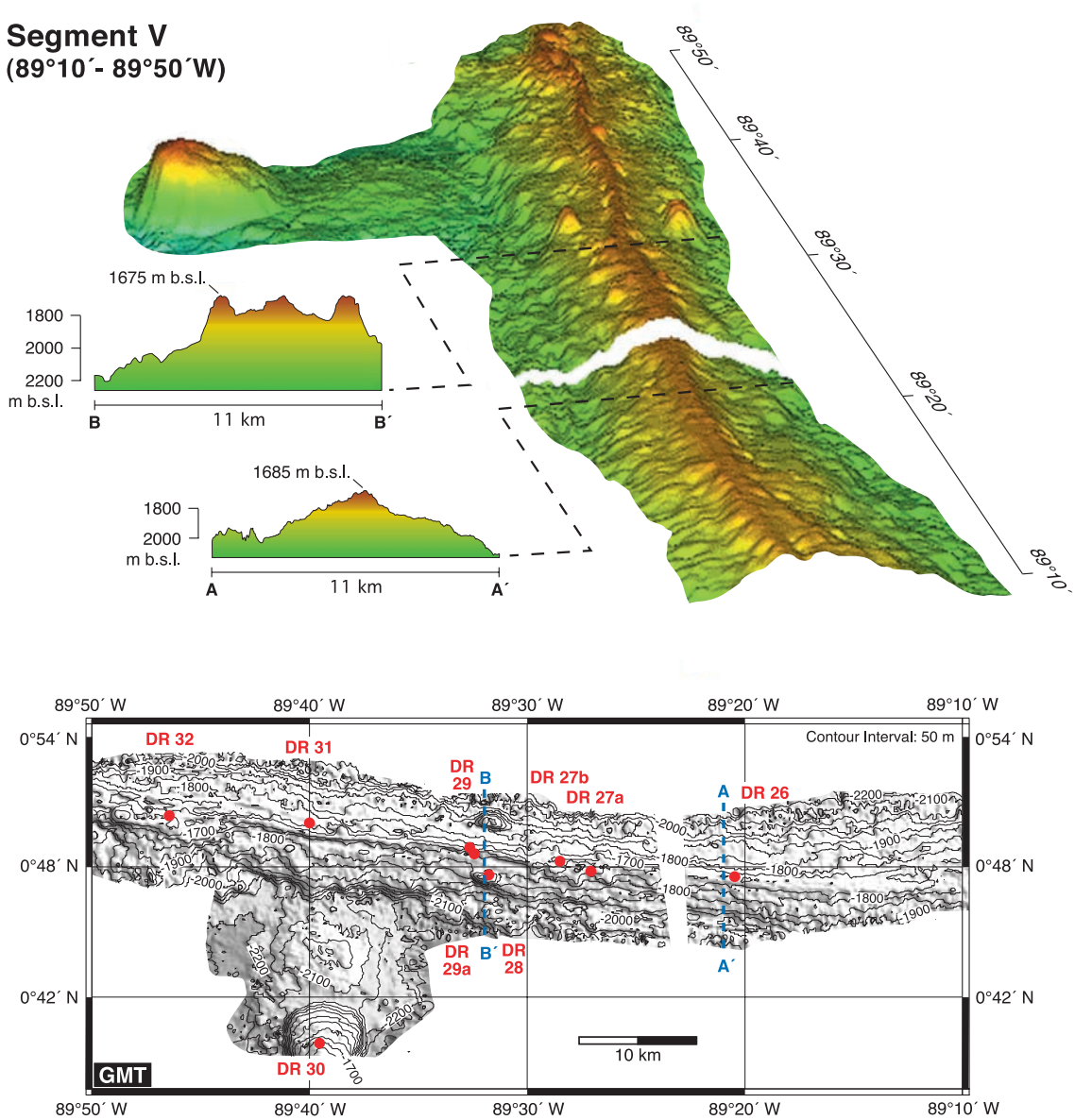

Figure 8. The easternmost axial ridge Segment V is characterized by a relatively uniform axial ridge with a continuous narrow crest and no axial summit graben. The width and volume of the axial ridge increase to the west, but its elevation is constant at 1,680 ± ~25 mbsl. Segment V includes two prominent seamounts: an approximately 250-m-high rifted axial volcano (split seamount) at 89°32′W and a 500-m-high, 7-km-diameter off-axis volcano ~18 km south of the ridge axis at 89°40′W. Red points and numbers indicate SO 158 dredge sites.

material inputs from the hot spot to the spreading system [e.g., *Schilling et al.*, 1976, 1982, 2003; *Verma et al.*, 1983]. These regional-scale gradients in isotopic ratios, incompatible trace element concentrations and ratios, and other parameters that reflect variations in source compositions and/or processes, are approximately symmetrical about, and clearly related to the influence of, the Galápagos hot spot on the GSC. In this section, we examine along-axis geochemical variability in some detail. We divide the seven morphologic segments of the eastern GSC into three distinct

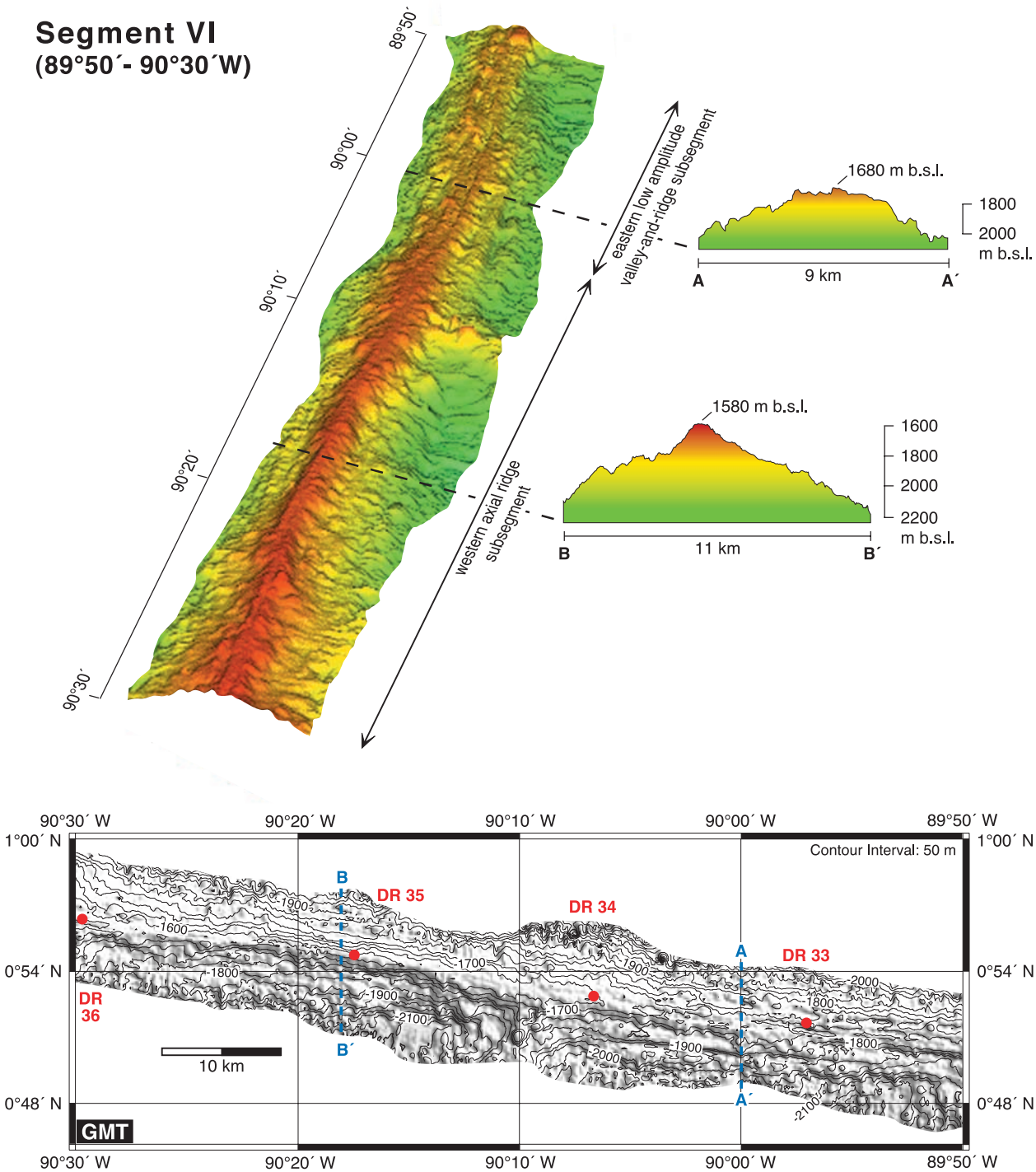

Figure 9. The axial ridge Segment VI consists of two contrasting subsegments. The eastern low-amplitude valley-and-ridge subsegment (89°50′–90°08′W) is transitional between the volcanic axial ridges of Segment V and the western subsegment of Segment VI. This transitional terrain consists of a broad axial high dissected by alternating ridges and grabens 100–300 m wide with 10- to 50-m vertical relief. Between 89°58′ and 90°08′W, a small OSC with ~3-km left-lateral offset separates the subsegments. Farther to the west, the crest of the southern limb of this OSC shoals from 1,680 to 1,500 mbsl, forming a relatively steep axial ridge with a narrow crest. At ~90°30′W the ridge crest broadens and flattens and the amplitude and volume of the axial ridge increases significantly. This transition marks the western end of Segment VI. Red points and numbers indicate SO 158 dredge sites.

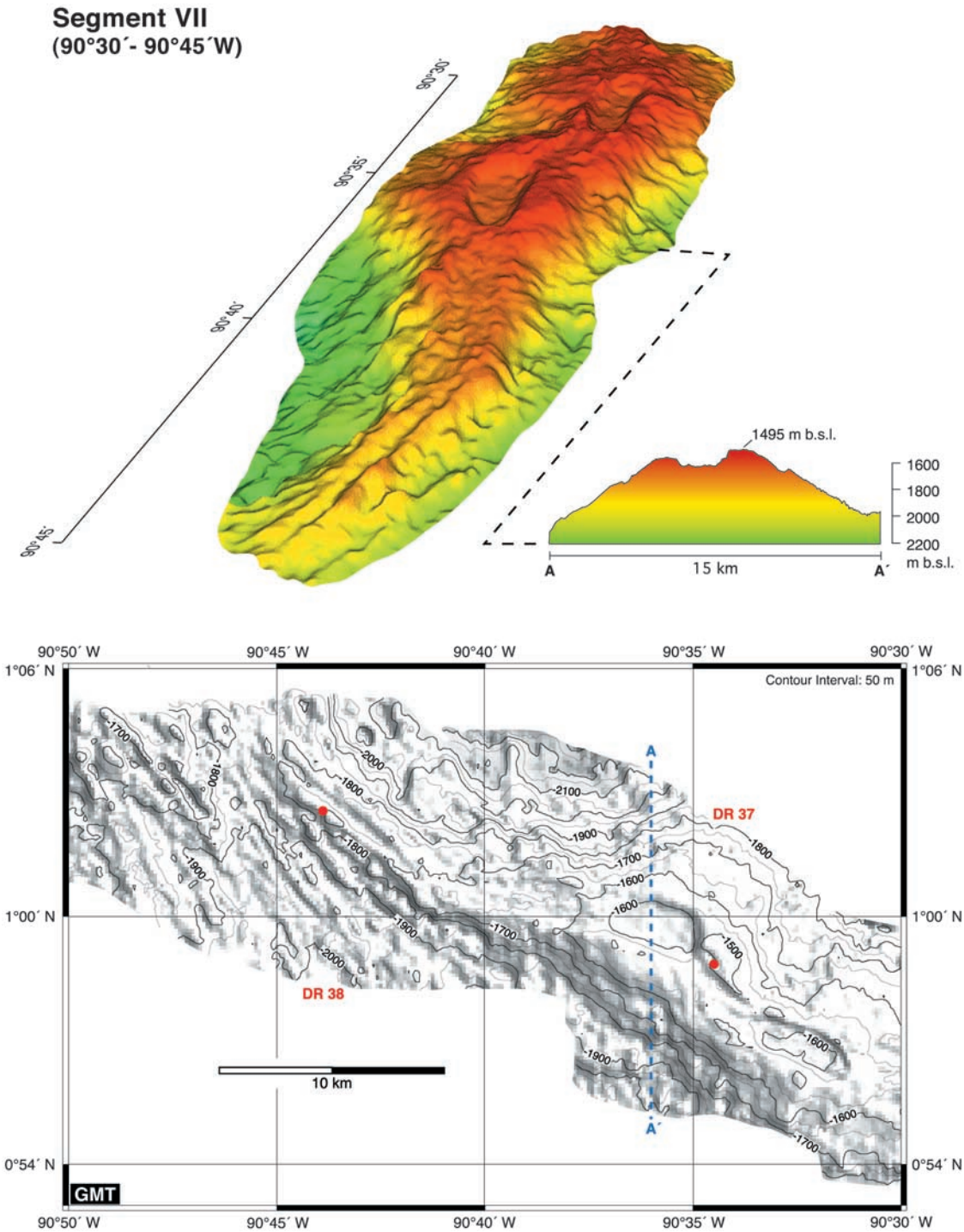

Figure 10. Segment VII is characterized by a voluminous axial ridge which consists of two broad overlapping volcanic shields that are more than 15 km wide and ~500 m high rising to less than 1,500 mbsl. Within each shield is an approximately 200-m-deep caldera (~5 × 2.5 km) that is elongate parallel to the ridge axis. The two calderas are arranged en echelon, separated by the only right-stepping offset between the Inca and 91°W transforms. The axial ridge extends ~10 km west of the northern (and western) caldera, decreasing in volume and increasing in depth but maintaining an axial graben. At 90°42′W, the ridge is only 4 km wide, shallowing to ~1,750 mbsl. Red points and numbers indicate SO 158 dredge sites.

magmatic segments within which most elements define coherent trends both along-axis and with decreasing MgO. These magmatic segments coincide closely with the axial morphology. They include a western, axial ridge domain (Segments V–VII), an eastern, valley-and-ridge domain (Segments I–III) and an intervening transitional domain (Segment IV).

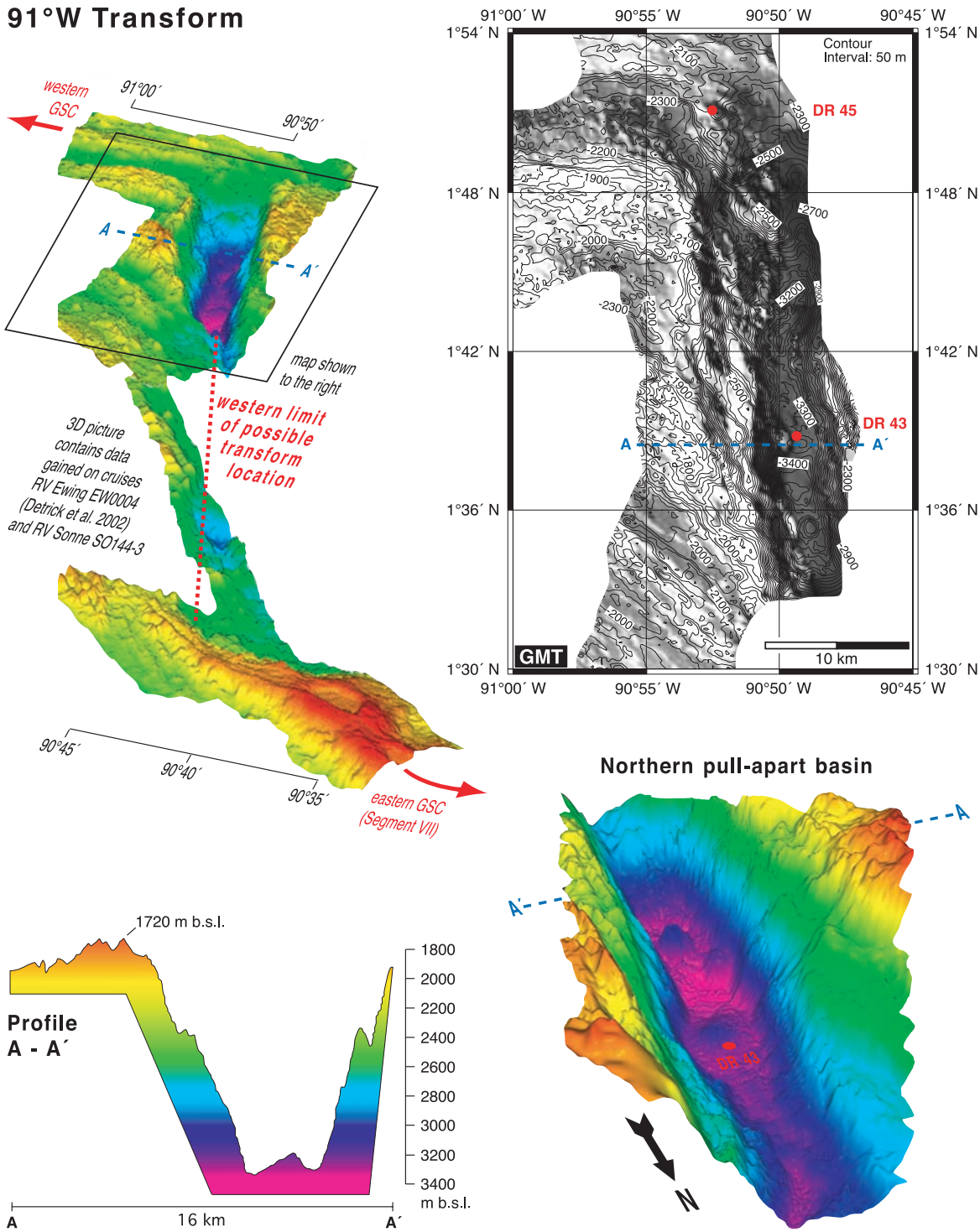

Figure 11

4.1. Correlations Between Morphology and Major and Minor Element Variability

[18] All eastern GSC lavas can be classified as mid-ocean ridge basalts (MORB) or their derivatives. In terms of K/Ti, they are predominantly transitional or T-MORB ($0.09 < K/Ti < 0.15$; as defined by *Detrick et al.* [2002] and *Cushman et al.* [2004] for the western GSC). Enriched or E-MORB lavas ($K/Ti > 0.15$) are present only along Segments V–VII. Maximum K/Ti values increase to the west, but they remain significantly lower (<0.20) than those from the western GSC (up to 0.44; Figure 12). The sole exception is an unusual seamount E-MORB, DR-28 with K/Ti = 0.56. The spatial distribution of E-MORB and N-MORB roughly mirrors that of the western GSC with a major peak in K/Ti and K_2O values near 91°50′W and a possible secondary peak near 90°30′W (Figure 12).

[19] In terms of their evolution, eastern GSC lavas are predominantly ferrobasalts (FeO > 12 wt.%) and FeTi basalts (FeO > 12 wt.% and TiO_2 > 2 wt.%). These highly evolved lavas occur on all segments but are rare in Segment V. Normal or N-MORB ($K/Ti < 0.09$) are generally less evolved (MgO > 7 wt.%, $TiO_2 < 2$ wt.%) and are present only on Segments I, III, and IV (Figure 12). The ranges of MgO and other major and minor elements are fairly constant from segment to segment (Figure 12). Only two SO 158 lavas are not basaltic. Two high-Si lavas ($SiO_2 \sim 55$ and ~52 wt.%) were recovered from the most inflated part of the eastern GSC, in the central region of Segment VI. These are off-scale in most of the figures. We did not encounter the abundant andesitic lavas previously reported from Segment I in the vicinity of 86°W by *Perfit and Fornari* [1983], *Fornari et al.* [1983], and *Perfit et al.* [1983]. It may be that our identification of the axis in this valley-and-ridge terrain differed from theirs, or it may be that new flows reported from the area by *Shank et al.* [2003] have buried the andesitic outcrops during the intervening 20+ years.

[20] Lavas of the eastern GSC can also be divided into two geochemically and geographically distinct populations that correlate with the principal axial morphologic domains. Geochemical contrasts between the two populations imply fundamental differences in magmatic evolution and, perhaps, in the array of primary melt compositions beneath the eastern and western regions. The western, "axial ridge" population is associated with the axial ridge terrain (Segments V–VII) that characterizes the GSC where it shoals toward the hot spot. It is characterized geochemically by (1) steeper along-axis gradients in the more incompatible elements and ratios; (2) complex magmatic histories that involve contributions from a broad array of parental compositions; and (3) MgO-variation trends for some of the more incompatible elements that are steeper than those predicted by simple crystallization models. Segment IV, with a subdued axial ridge that diminishes in amplitude to the east by ~100 m, is transitional in some aspects of its geochemistry, while in others it is clearly associated with the western axial ridge population. The eastern, "valley-and-ridge" population is associated with the transitional, low-amplitude (200–500 m) valley-and-ridge terrain (Segments I–III) and characterized geochemically by coherent, simple trends on MgO variation diagrams that are generally consistent with a dominant control by shallow crystal fractionation. Segment IV lies between these two populations and has attributes of both.

Figure 11. Shaded relief images, map, and cross section of the 91°W transform and adjacent ridge segments based on merged multibeam bathymetry from cruises SO 158 and EW0004 [*Detrick et al.*, 2002; *Sinton et al.*, 2003]. Red points and numbers indicate SO 158 dredge sites. The northern part of the 91°W transform is a NNW-SSE trending pull-apart basin 3,500 m deep, approximately 35 km long, and approximately 12 km wide, bounded to the north by the steep southern slope of the eastern tip of the western GSC and by very steep eastern and western slopes. Note the two small, approximately 200- and 400-m-high volcanic cones on its floor, which are probably active, because very fresh, glassy volcanic rocks were recovered from their flanks during cruises EW0004 [*Detrick et al.*, 2002; *Sinton et al.*, 2003] and SO 158 (DR 43). To the south, the basin narrows and shoals less steeply into a narrow, relatively shallow graben that trends SSE beyond the map coverage. Farther to the south, the geometry of the transform is undefined, and there is no recognizable transform intersection along Segment VII. However, the single multibeam swath connecting Segment VII to the off-axis terrain southwest of the known transform deep defines the western limit for possible transform locations. The well-developed NW-SE seafloor fabric along the northern half of this line must lie to the west of the southern transform and therefore defines its western limit. The northwest continuation of this oblique terrain suggests that deformation associated with the 91°W offset may be partly accommodated along oblique faults. Segment VII of the eastern GSC extends to the west of all possible transform locations and bends north into this oblique terrain.

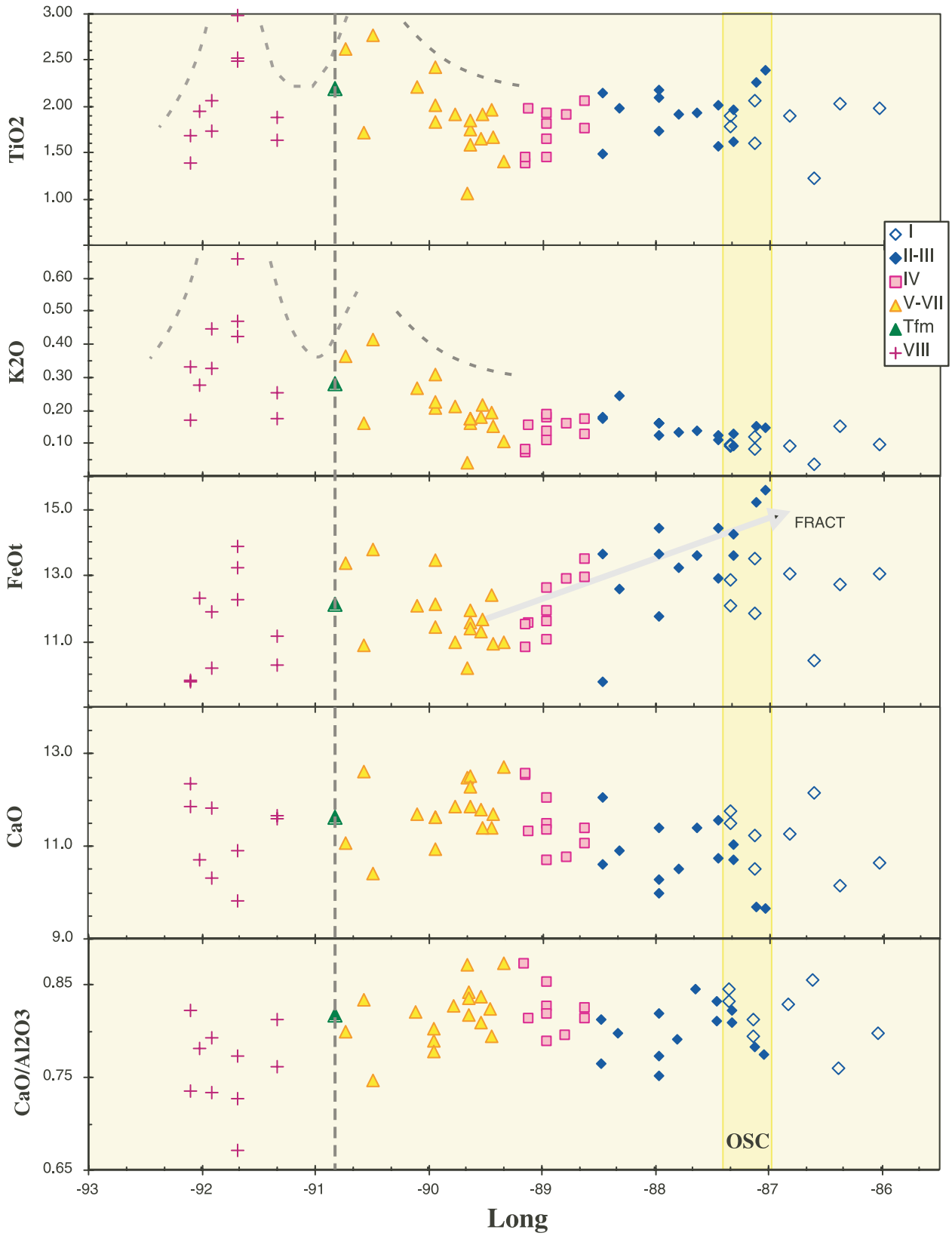
TiO2
K2O
FeOt
CaO
CaO/Al2O3
Long
FRACT
OSC
I
II-III
IV
V-VII
Tfm
VIII

Figure 12

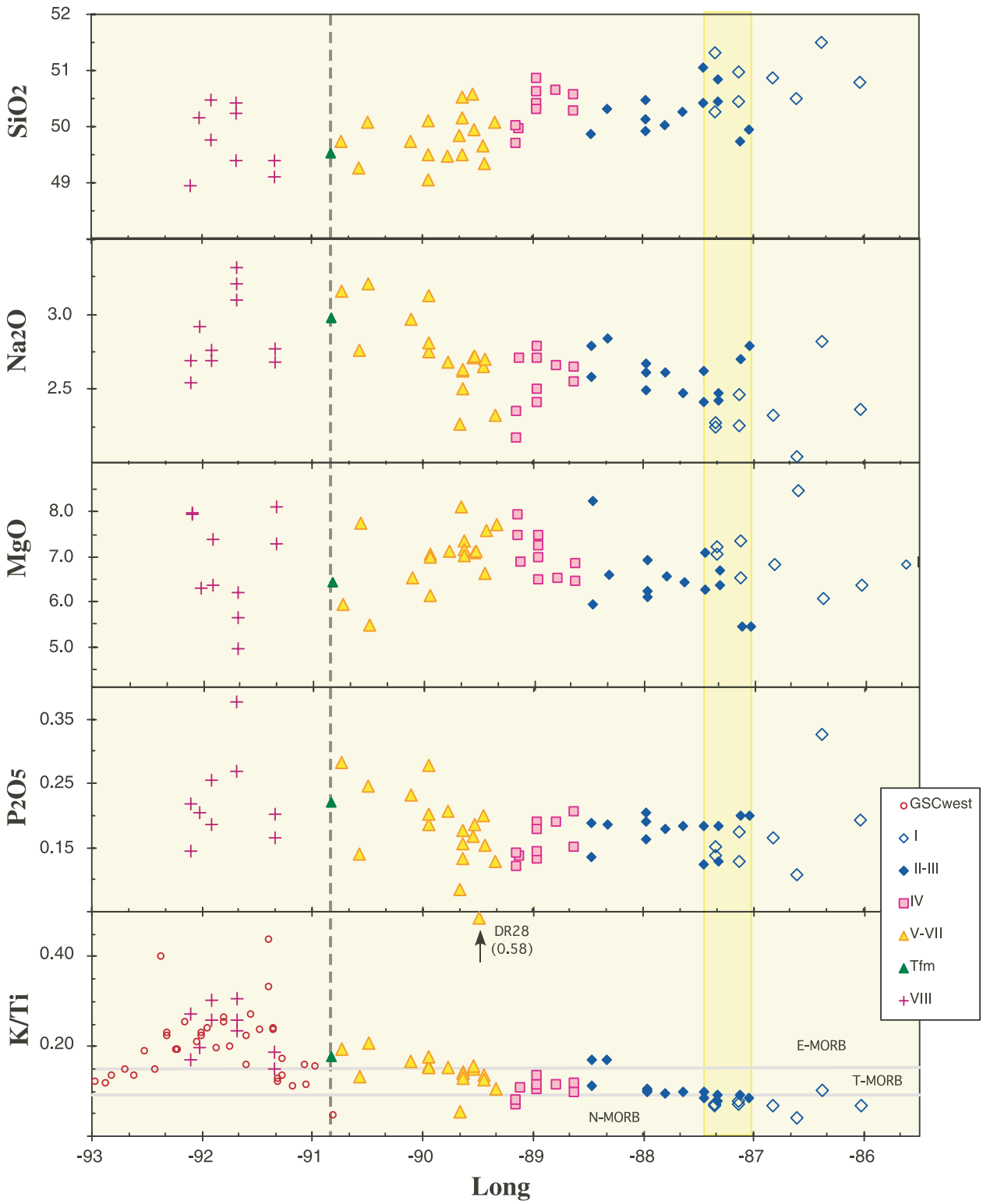

Figure 12. (continued)

[21] In MgO variation diagrams (Figure 13, Table 2), the axial ridge segments display steeper trends and higher values for the more incompatible elements than the valley-and-ridge segments. In some cases, including K_2O, TiO_2, Sr, and La (but not Yb), these trends are steeper than those predicted for simple crystal fractionation at crustal depths. This type of "over-enrichment" trend was described by *Sours-Page et al.* [1999]. The development of such trends has been interpreted to require a complex melting and/or extraction process, from which a range of variably enriched primary magmas can migrate to shallow depth. The more enriched a primary magma batch, the more it tends to evolve by shallow crystal fractionation.

[22] For most elements and ratios, regional gradients, usually defined by the maximum value at any given longitude, are clearly defined. In considering these gradients, however, it is important to keep in mind that a significant range of lava compositions is present at all points along the GSC, reflecting persistent variability in source compositions and/or processes. The along-axis gradients differ from element to element (or ratio), but most fall into one of two groups (Figure 12 and 14; Tables 3a and 3b). For the first group, abundances and ratios of (incompatible) elements that primarily reflect source compositions or processes increase gradually to the west along the valley-and-ridge segments (I–III), and much more steeply along the axial ridge segments (V–VII). Examples include Na_2O, K_2O, K/Ti, Nb/Zr, La/Sm, and La/Yb. Ba/Nb increases monotonically from Segment III to VI and Na_8 along the entire eastern GSC (Figures 14 and 15d). For certain other parameters, including Ca, Al, Ca/Al, P_2O_5, and perhaps MgO, along-axis gradients change direction. Typically, these values decrease overall from east to west along Segment II, increase steeply along Segments III and IV, and flatten or decrease along Segments VI and VII. These monotonic intersegment and intrasegment gradients are inconsistent with focusing of magma supply at segment centers. They reflect a linearly distributed magma supply system that is tapping a gradient in thermally and/or compositionally dominated melting effects approaching the hot spot. Superimposed, localized, element-to-element inconsistencies perturb the regional pattern, suggesting transient variations in magma supply, melting parameters, and/or source composition.

[23] Geochemical gradients are known to peak in the vicinity of the hot spot, but the segment-scale shapes and locations of these peaks have not been examined in any detail. The western GSC data of *Detrick et al.* [2002], *Sinton et al.* [2003], and *Cushman et al.* [2004] show a distinct peak in many parameters at ~91°50′W. Our data strongly suggest that there is a second, less clearly defined peak near 91°30′W. The eastern and western peaks vary in magnitude from element to element (Figure 12 and 14). K_2O, TiO_2, La/Sm, and perhaps La/Yb, all show double peaks, while K_2O/TiO_2 and Nb/Zr, which are enriched in E-MORB, reach regional highs near 91°50′W with only indistinct peaks at ~90°30′W. In our data, La/Yb reaches a regional high near 90°30′W with a smaller peak near 91°50′, but the addition of two data points from *Schilling et al.* [1982] makes this pattern much less clear. These local peaks are of particular interest because they reflect patterns of material flow from the Galápagos plume to the spreading axis. Their nature and significance is discussed in more detail in section 5.1.

[24] Both maximum and minimum SiO_2 contents of basalt glasses decrease monotonically from east to west along the entire eastern GSC, although SiO_2 varies randomly with MgO, precluding a meaningful calculation of parental SiO_2 variability. Nevertheless, an overall decrease in primary SiO_2 content is consistent with models involving decreasing extents of melting in the presence of increasing mantle H_2O approaching the Galápagos hot spot [*Detrick et al.*, 2002; *Asimow and Langmuir*, 2003; *Cushman et al.*, 2004] (see later discussion).

[25] Variations in elements that serve as fractionation indices are likewise inconsistent along the eastern GSC. The peak in FeO and TiO_2, defined by data of *Perfit and Fornari* [1983] from 85.5°W – 86°W and considered a definitive characteristic of the 85.5°W propagating rift by *Sinton et al.* [1983], is not apparent in the SO 158 data, perhaps

Figure 12. Along-axis variations in major element contents and ratios for all analyzed SO 158 basaltic glasses. The E-MORB lava DR 28 and two high-silica lavas are omitted as they plot off-scale in most diagrams. Roman numerals in legend are segment numbers discussed in text and illustrated in Figures 2–11. Tfm refers to the 91°W transform. Segment VIII refers to SO 158 samples from the between approximately 91°W and 92°15′W. GSCwest refers to data of *Detrick et al.* [2002] and *Cushman et al.* [2004] included only in the K/Ti diagram. Curved dashed lines outline geochemical peaks. Vertical dashed line indicates the location of the northern basin of the 91°W transform.

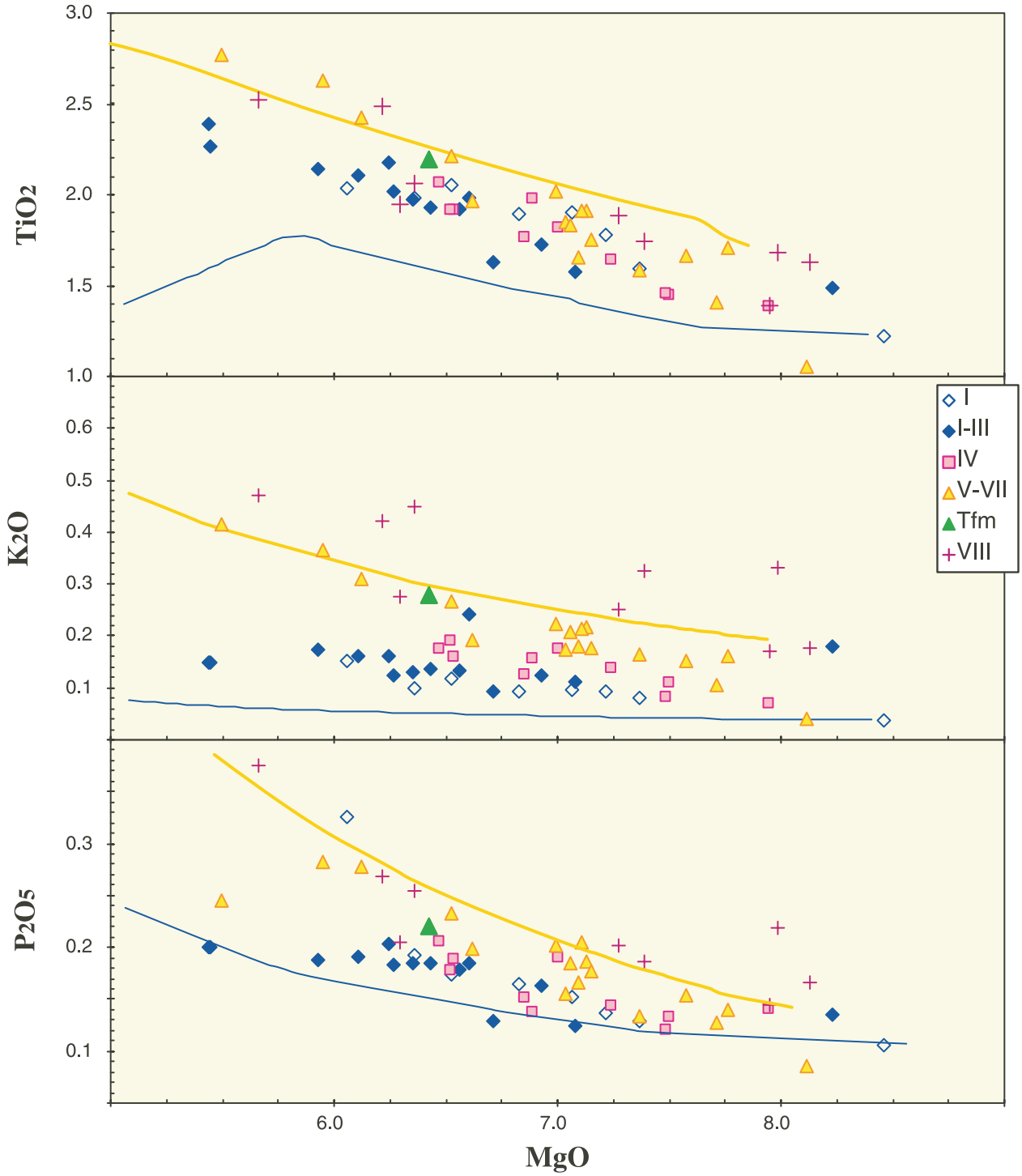

Figure 13. MgO variation diagrams for selected major element concentrations for all analyzed SO 158 basaltic glasses except DR 28. Symbols as for Figure 12. Lines are liquid lines of descent (LLD) modeled for 1 atm. pressure using the COMAGMAT program of *Ariskin et al.* [1993] and parent compositions from DR 7 and DR 37. In some cases the lines have been shifted slightly up or down for visibility.

reflecting our low sampling density in this region. From Segment V through Segment II, however, a gradual increase in both maximum and minimum FeO values to the east, away from the hot spot, accompanies decreases in CaO, MgO, and mg# (Figure 12). That is, both mean and maximum extents of fractionation increase uniformly over almost 300 km from the western end of Segment

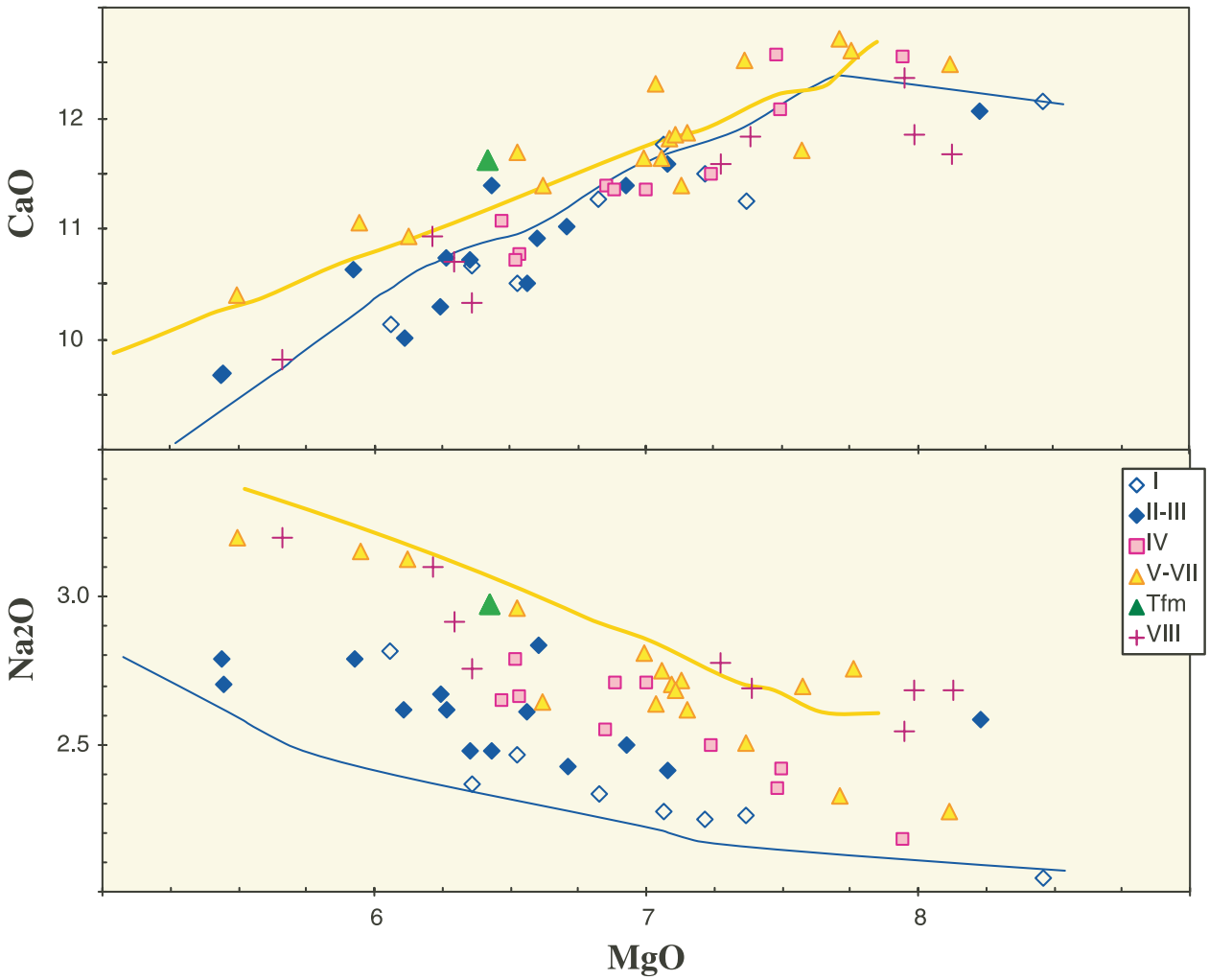

Figure 13. (continued)

V to the eastern, propagating tip of Segment II. The direction of this fractionation effect is consistent with the long-term, rapid eastward propagation of the 87°W OSC first documented by *Hey* [1977], but the other key indicators of rift propagation at 95.5°W and 85.5°W [*Christie and Sinton*, 1981; *Sinton et al.*, 1983] are not apparent. These include abrupt (over a few tens of km) increases in FeO, TiO_2, and other fractionation indicators (including decreases in MgO and mg#), the presence of unfractionated lavas at the propagating rift tip, and the characteristic increase in axial depth at the propagating tip. The 93°15′W propagating OSC also lacks the pronounced signature of the two outer Galápagos propagating rifts. *Sinton et al.* [2003] concluded that this absence results from a reduction in the thermal contrast between the propagating tip and its surroundings due to a combination of increased magma supply and a shorter offset distance. In this "warmer" environment, the balance between magma supply and cooling rate [*Christie and Sinton*, 1981] is shifted away from conditions conducive to crystal fractionation.

[26] Additional complications associated with propagation of an OSC, as opposed to the simpler propagating rift geometry of 95.5°W, are suggested by along-axis trends in FeO, MgO, and mg# approaching the 87°W OSC, at the western end of Segment I. In the long term, Segment I is failing as Segment II propagates to the east [*Hey*, 1977]. On a shorter timescale, however, the geochemical data confirm the morphological inference (section 3.2) that the multiple branches of Segment I reflect multiple, transient westward propagation events. Along the western subsegment of Segment I, both the maximum degree of fractionation, as indicated by high FeO, low MgO, and low mg#, and the overall ranges of these parameters increase initially

Table 2. Group Average Major Element Analyses for SO 158 Basalt Glasses[a]

Group[b]	Latitude, °N	Longitude, °W	Depth, m	SiO_2	TiO_2	Al_2O_3	FeOt	MnO	MgO	CaO	Na_2O	K_2O	P_2O_5	Total
						Segments I–III								
SO 3	0.78	−86.03	2458	50.78	1.98	13.34	13.04	0.21	6.36	10.66	2.36	0.10	0.19	99.02
SO 6	0.83	−86.39	2423	51.50	2.03	13.35	12.73	0.20	6.06	10.14	2.81	0.15	0.33	99.30
SO 7	0.85	−86.61	2415	50.50	1.22	14.19	10.42	0.22	8.46	12.14	2.05	0.04	0.11	99.35
SO 8	0.87	−86.83	2379	50.88	1.89	13.58	13.04	0.19	6.83	11.26	2.33	0.09	0.16	100.26
SO 9Z	0.88	−87.14	2433	50.96	1.60	13.83	11.87	0.20	7.37	11.25	2.26	0.08	0.13	99.55
SO 9Y	0.88	−87.14	2433	50.44	2.06	13.23	13.50	0.21	6.53	10.51	2.46	0.12	0.17	99.22
SO 10Z	0.87	−87.35	2467	50.27	1.78	13.81	12.10	0.19	7.22	11.49	2.25	0.09	0.14	99.32
SO 10Y	0.87	−87.35	2467	51.32	1.90	13.93	12.87	0.18	7.07	11.77	2.27	0.09	0.15	101.56
SO 11	0.77	−87.05	2268	49.94	2.39	12.49	15.60	0.24	5.44	9.67	2.79	0.15	0.20	98.90
SO 12	0.76	−87.13	2229	49.74	2.27	12.39	15.21	0.22	5.45	9.69	2.71	0.15	0.20	98.01
SO 13X	0.70	−87.33	2240	51.52	1.48	17.28	11.64	0.18	5.01	10.64	2.52	0.10	0.21	100.57
SO 13Z	0.70	−87.33	2240	50.84	1.62	13.41	13.60	0.20	6.71	11.02	2.43	0.09	0.13	100.07
SO 13Y	0.70	−87.33	2240	50.44	1.97	13.22	14.27	0.21	6.35	10.71	2.48	0.13	0.18	99.96
SO 14Z	0.70	−87.46	2282	51.05	1.57	13.91	12.92	0.21	7.08	11.58	2.41	0.11	0.12	100.97
SO 14Y	0.70	−87.46	2282	50.43	2.01	13.22	14.42	0.22	6.27	10.73	2.62	0.12	0.18	100.24
SO 15b	0.70	−87.64	2202	50.26	1.93	13.47	13.62	0.23	6.43	11.39	2.48	0.14	0.18	100.12
SO 16	0.73	−87.80	2197	50.03	1.92	13.26	13.25	0.22	6.56	10.50	2.61	0.13	0.18	98.65
SO 17Z	0.72	−87.97	2174	50.46	1.73	13.89	11.78	0.22	6.93	11.39	2.49	0.12	0.16	99.19
SO 17Y	0.72	−87.97	2174	49.91	2.18	13.31	13.65	0.24	6.24	10.29	2.67	0.16	0.20	98.87
SO 17X	0.72	−87.97	2174	50.12	2.10	13.31	14.44	0.23	6.11	10.00	2.61	0.16	0.19	99.28
SO 19	0.75	−88.33	1970	50.31	1.98	13.67	12.58	0.24	6.60	10.90	2.83	0.24	0.19	99.55
SO 21Z	0.75	−88.47	1998	47.85	1.49	15.76	9.76	0.16	8.23	12.07	2.58	0.18	0.14	98.21
SO 21Y	0.75	−88.47	1998	49.86	2.14	13.06	13.66	0.22	5.93	10.62	2.79	0.17	0.19	98.64
						Segment IV								
SO 22Z	0.76	−88.63	1838	50.59	1.77	13.78	12.95	0.19	6.85	11.39	2.55	0.13	0.15	100.36
SO 22Y	0.76	−88.63	1838	50.29	2.07	13.59	13.53	0.21	6.47	11.07	2.65	0.18	0.21	100.26
SO 23	0.78	−88.80	1767	50.65	1.92	13.52	12.91	0.20	6.53	10.77	2.66	0.16	0.19	99.52
SO 24Z	0.80	−88.97	1807	50.63	1.45	14.13	11.09	0.17	7.49	12.07	2.42	0.11	0.13	99.70
SO 24Y	0.80	−88.97	1807	50.43	1.65	13.90	11.62	0.19	7.24	11.50	2.50	0.14	0.14	99.31
SO 24X	0.80	−88.97	1807	50.32	1.82	13.85	11.95	0.21	7.00	11.36	2.71	0.18	0.19	99.60
SO 24W	0.80	−88.97	1807	50.87	1.92	13.58	12.65	0.24	6.52	10.72	2.79	0.19	0.18	99.66
SO 25	0.80	−89.13	1753	49.97	1.99	13.95	11.60	0.23	6.89	11.35	2.71	0.16	0.14	98.97
SO 25aZ	0.81	−89.16	1780	49.70	1.39	13.89	10.84	0.19	7.94	12.55	2.18	0.07	0.14	98.90
SO 25aY	0.81	−89.16	1780	50.02	1.46	14.39	11.53	0.20	7.48	12.58	2.35	0.08	0.12	100.21
						Segments V–VII								
SO 26	0.79	−89.34	1704	50.09	1.41	14.56	10.99	0.16	7.71	12.71	2.32	0.11	0.13	100.19
SO 27	0.80	−89.45	1708	49.67	1.96	13.83	12.40	0.21	6.62	11.39	2.65	0.19	0.20	99.11
SO 27a	0.80	−89.44	1702	49.34	1.67	14.72	10.93	0.19	7.57	11.70	2.70	0.15	0.15	99.12
SO 28	0.80	−89.53	1767	48.98	1.98	16.78	8.08	0.14	8.13	11.11	2.86	0.83	0.36	99.23
SO DR29-1.	0.82	−89.54	1713	50.57	1.65	14.11	11.29	0.22	7.09	11.81	2.71	0.18	0.17	99.80

Table 2. (continued)

Group[b]	Latitude, °N	Longitude, °W	Depth, m	SiO_2	TiO_2	Al_2O_3	FeOt	MnO	MgO	CaO	Na_2O	K_2O	P_2O_5	Total
						Segments I–III								
SO 29a	0.81	−89.54	1687	49.95	1.91	14.08	11.68	0.21	7.13	11.39	2.72	0.22	0.19	99.47
SO 30	0.67	−89.66	1709	49.85	1.06	14.32	10.19	0.19	8.12	12.49	2.27	0.04	0.09	98.61
SO 31Z	0.83	−89.64	1811	50.15	1.58	14.86	11.58	0.18	7.37	12.52	2.50	0.16	0.13	101.04
SO 31Y	0.83	−89.64	1811	49.50	1.75	14.49	11.39	0.19	7.15	11.86	2.62	0.18	0.18	99.30
SO 31X	0.83	−89.64	1811	50.53	1.85	14.72	11.94	0.21	7.03	12.31	2.64	0.17	0.15	101.55
SO 32	0.84	−89.77	1680	49.47	1.91	14.31	10.98	0.20	7.11	11.85	2.68	0.21	0.21	98.94
SO 33Z	0.86	−89.95	1755	49.05	1.84	14.50	11.45	0.20	7.06	11.63	2.75	0.21	0.19	98.86
SO 33Y	0.86	−89.95	1755	49.50	2.02	14.72	12.15	0.20	6.99	11.63	2.81	0.22	0.20	100.45
SO 33X	0.86	−89.95	1755	50.12	2.42	14.05	13.45	0.23	6.12	10.93	3.13	0.31	0.28	101.04
SO 34	0.88	−90.11	1642	49.73	2.22	14.25	12.09	0.20	6.53	11.69	2.96	0.27	0.23	100.16
SO 35	0.91	−90.29	1583	52.07	2.86	13.26	13.53	0.24	4.01	8.10	3.81	0.59	0.50	98.97
SO 36Y	0.94	−90.50	1557	55.44	2.51	13.49	13.07	0.24	2.97	7.02	4.40	0.83	0.71	100.68
SO 36Z	0.94	−90.50	1557	50.09	2.77	13.94	13.78	0.23	5.50	10.40	3.20	0.42	0.25	100.55
SO 37	0.98	−90.58	1501	49.27	1.71	15.13	10.89	0.20	7.76	12.61	2.76	0.16	0.14	100.63
SO 38	1.04	−90.73	1717	49.73	2.63	13.84	13.36	0.19	5.95	11.06	3.15	0.36	0.28	100.55
						91°W Transform								
SO 43	1.65	−90.82	3302	49.51	2.19	14.20	12.11	0.19	6.42	11.62	2.97	0.28	0.22	99.72
						Segment VIII (GSCwest)								
SO 48Z	1.93	−91.34	1594	49.12	15.32	1.63	10.30	0.18	8.13	11.68	2.69	0.18	0.17	99.38
SO 48Y	1.93	−91.34	1594	49.39	1.88	14.25	11.15	0.23	7.27	11.59	2.77	0.25	0.20	99.00
SO 49Z	2.06	−91.69	1786	49.39	2.49	14.12	12.27	0.18	6.22	10.92	3.10	0.42	0.27	99.37
SO 49Y	2.06	−91.69	1786	50.24	2.52	13.49	13.21	0.24	5.66	9.81	3.20	0.47	0.38	99.23
SO 49X	2.06	−91.69	1786	50.41	2.99	13.33	13.88	0.23	4.96	8.95	3.31	0.66	0.44	99.16
SO 53Z	2.11	−91.91	1705	49.76	1.74	14.92	10.18	0.17	7.39	11.83	2.69	0.33	0.19	99.18
SO 53Y	2.11	−91.91	1705	50.47	2.06	14.05	11.91	0.21	6.36	10.32	2.76	0.45	0.25	98.85
SO 54Z	2.11	−92.11	1727	48.95	1.39	15.04	9.80	0.15	7.95	12.36	2.54	0.17	0.15	98.51
SO 54Y	2.11	−92.11	1727	47.71	1.68	16.11	9.84	0.16	7.99	11.85	2.69	0.33	0.22	98.56
SO 56	2.11	−92.02	1877	50.16	1.95	13.70	12.30	0.22	6.29	10.70	2.92	0.28	0.20	98.73

[a] Individual analyses are averages of 3–5 replicate points on glass chips separated on board from as many individual pieces as possible in each dredge. Analyses by Chris Russo and Roger Nielsen using Cameca Sx V electron microprobe at Oregon State University.

[b] A chemical group is empirically defined to include all samples from a single dredge for which compositions vary by less than analytical error. Analyses in this table are averages of individual analyses of all glasses included in each group.

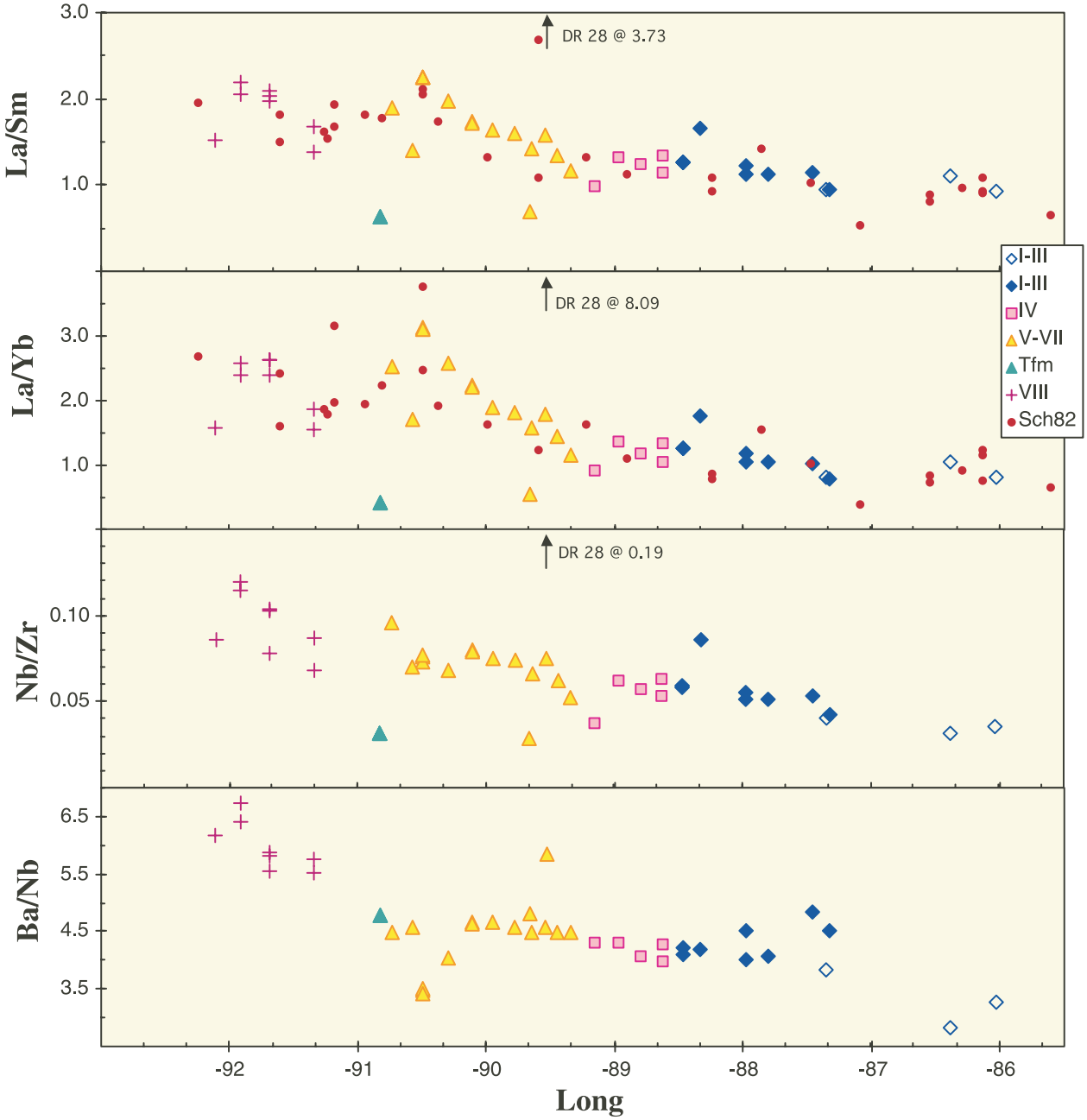

Figure 14. Along-axis variations in selected trace element ratios for all analyzed SO 158 volcanic glasses. Symbols as in Figure 12.

westward then decrease near the rift tip (Figure 12), a pattern common to a number of active propagating rifts [*Christie and Sinton*, 1981; *Sinton et al.*, 1983].

4.2. Correlations Between Morphology and Trace Element Variability

[27] Lavas from the axial ridge segments of the eastern GSC are distinct from those of the valley-and-ridge segments in their generally higher incompatible trace element contents and ratios and especially in their higher overall variability. Along the axial ridge segments (V–VII), many parameters show an extended range at a given longitude, at a given MgO value or within an individual segment. This is well illustrated by the rare earth elements (Figures 16 and 17). Lavas from the valley-and-ridge segments (I–III) have the depleted REE patterns of typical MORB, with a narrow range of chondrite normalized La/Sm values (La/Sm(n), 0.58–1.03). If we exclude a single T-MORB lava from dredge DR19 (see section 5.2), the max-

Table 3a. Light Trace Element Analyses for Individual SO 158 Basalt Glasses[a]

Segment	Sample ID	Group	Lat	Long	Depth	Sc	V	Cr	Co	Ni	Zn	Rb	Sr	Y	Zr	Nb	Cs
I	DR 3-1b	SO 3	0.78	−86.03	2458	44.8	416	82	44	53	123	2.0	62	58	146	5.1	0.05
I	DR 6-2	SO 6	0.83	−86.39	2423	39.6	354	216	41	203	106	2.5	61	79	264	8.2	0.04
I	DR10-2	SO 10Y	0.87	−87.35	2467	42.6	378	303	47	96	104	1.8	60	44	105	4.3	0.04
II	DR13-4	SO 13Z	0.70	−87.33	2240	47.6	413	53	50	42	114	1.8	67	43	94	3.9	0.05
II	DR14-1	SO 14Z	0.70	−87.46	2282	46.9	385	88	49	49	105	2.4	77	40	95	5.1	0.05
II	DR16-1	SO 16	0.73	−87.80	2197	46.5	416	64	49	44	118	2.7	78	49	122	6.2	0.05
II	DR17-2	SO 17Y	0.72	−87.97	2174	44.7	434	50	50	45	125	3.2	82	52	138	7.6	0.06
II	DR17-21	SO 17Z	0.72	−87.97	2174	45.8	368	66	46	51	101	2.3	85	40	102	5.2	0.05
II	DR18-1	SO 18	0.73	−88.14	2120	47.8	402	44	49	49	112	3.0	95	47	123	7.1	0.06
III	DR19-1	SO 19	0.75	−88.33	1970	44.5	382	43	47	42	109	5.2	119	44	134	11.5	0.08
III	DR21-1	SO 21Z	0.75	−88.47	1998	45.4	412	62	49	46	118	3.2	89	49	131	7.6	0.05
III	DR21-4	SO 21Y	0.75	−88.47	1998	46.8	430	44	49	43	124	3.6	95	52	143	8.4	0.06
IV	DR22-10	SO 22Z	0.76	−88.63	1838	44.3	376	74	46	48	104	2.4	74	42	106	5.7	0.04
IV	DR22-2	SO 22Y	0.76	−88.63	1838	45.6	397	60	47	46	114	3.5	95	47	129	8.1	0.06
IV	DR23-2	SO 23	0.78	−88.80	1767	46.7	408	57	48	46	115	3.0	86	48	127	7.3	0.06
IV	DR24-1	SO 24X	0.80	−88.97	1807	45.2	364	105	47	62	104	3.2	98	44	122	7.5	0.06
IV	DR25a-1	SO 25aZ	0.81	−89.16	1780	48.0	332	204	48	102	89	1.5	91	36	92	3.4	0.04
V	DR26-2	SO 26	0.79	−89.34	1704	44.7	316	251	47	87	85	2.0	88	34	87	4.6	0.04
V	DR27a-1	SO 27a	0.80	−89.44	1702	44.1	323	250	48	83	92	2.9	116	37	109	6.7	0.05
V	DR28[d]	SO 28	0.80	−89.53	1767	34.2	255	295	43			18	376	28	188	37	0.23
V	DR29a-1	SO 29a	0.81	−89.54	1687	43.5	356	150	46	63	101	4.3	119	41	128	9.6	0.07
V	DR30-5	SO 30	0.67	−89.66	1709	48.0	310	182	50	81	81	0.7	67	29	52	1.5	0.03
V	DR31-4	SO 31Y	0.83	−89.64	1811	45.0	337	222	47	78	96	3.3	111	39	114	7.5	0.06
V	DR32-1	SO 32	0.84	−89.77	1680	44.2	341	209	47	75	99	4.1	118	40	125	9.3	0.07
VI	DR33-2	SO 33Y	0.86	−89.95	1755	42.3	339	212	47	82	100	4.4	131	40	130	9.8	0.07
VI	DR34-11	SO 34	0.88	−90.11	1642	44.8	365	139	47	59	108	5.4	160	44	153	12.2	0.07
VI	DR34-3	SO 34	0.88	−90.11	1642	44.0	363	125	46	55	107	5.4	157	44	153	12.2	0.07
VI	DR35-1	SO 35	0.91	−90.29	1583	33.5	275	18	34	16	145	12.4	146	83	422	28.7	0.15
VI	DR36-2	SO 36Y	0.94	−90.50	1557	25.5	113	33	26	9	135	18.2	159	115	677	51.8	0.22
VI	DR36-4	SO 36Y	0.94	−90.50	1557	26.4	112	34	27	11	139	18.7	163	119	719	52.8	0.21
VI	DR36-5	SO 36Z	0.94	−90.50	1557	25.9	117	36	26	15	135	18.0	159	114	672	51.5	0.19
VII	DR37-1	SO 37	0.98	−90.58	1501	45.0	303	258	46	81	85	3.1	141	35	106	7.4	0.05
VII	DR38-1	SO 38	1.04	−90.73	1717	42.3	381	90	45	51	121	7.2	171	49	177	17.0	0.09
Tfm	DR43-1	SO 43	1.65	−90.82	3302	44.8	311	400	49	123	82	0.7	46	28	43	1.4	0.03
Tfm	DR43-2	SO 43	1.65	−90.82	3302	44.8	311	400	49	123	82	0.7	46	28	43	1.4	0.03
VIII	DR48-1	SO 48Y	1.93	−91.34	1594	45.5	334	203	47	83	92	5.3	141	39	119	10.3	0.10
VIII	DR48-4	SO 48Z	1.93	−91.34	1594	43.3	312	267	48	108	86	3.5	142	36	106	7.3	0.07
VIII	DR49-1	SO 49Y	2.06	−91.69	1786	42.9	417	24	43	31	123	10.7	158	54	189	19.5	0.14
VIII	DR49-2	SO 49X	2.06	−91.69	1786	39.8	406	15	39	26	138	15.2	166	69	350	27.3	0.19
VIII	DR49-4	SO 49Z	2.06	−91.69	1786	45.3	378	94	43	49	107	9.6	187	46	170	17.5	0.13
VIII	DR53-1	SO 53Y	2.11	−91.91	1705	42.0	364	101	43	57	103	10.5	155	44	152	18.1	0.14
VIII	DR53-3	SO 53Z	2.11	−91.91	1705	44.1	325	231	46	83	91	7.4	163	35	111	12.7	0.10
VIII	DR54-1	SO 54Z	2.11	−92.11	1727	47.0	303	397	47	96	80	3.9	129	32	83	7.1	0.06

Table 3. (continued)

Segment	Sample ID	Group	Lat	Long	Depth	Sc	V	Cr	Co	Ni	Zn	Rb	Sr	Y	Zr	Nb	Cs
K1919 average of 5 repeats[b]				31.6	318.8	258.1	53.9	102.1	111.5	9.9	427.4	29.1					
StDev								0.3	3.0	2.6	0.8	0.9	1.1	0.1	5.0	0.4	
BHVO accepted[c]							31.8	317	289	45	121	105	11	403	27.6		

[a] All values in ppm. Solution ICP-MS analyses by Chris Russo in the W.M. Keck Collaboratory for Plasma Spectrometry at Oregon State University (http://wmkeck-icpms.coas.oregonstate.edu/).
[b] Average of 5 replicates, run with samples, of rock standard K1919, equivalent to USGS standard BHVO-1.
[c] *Govindaraju* [1989] accepted values for BHVO-1.
[d] DR 28 analysis is average for 3 replicates each of 5 chips by Excimer laser ablation ICP-MS by Adam Kent using techniques of *Kent et al.* [2004].

imum La/Sm(n) is only 0.86. Lavas from the axial ridge segments (V–VII) have a wide range of REE patterns, ranging from slightly more depleted (La/Sm(n), 0.56) than those of the valley-and-ridge segments, to markedly more enriched (La/Sm(n), 1.21). Heavy REE concentrations are lower in the axial ridge lavas, while La/Yb ratios more than double from Segment IV to Segment VII (Figures 14 and 15d). The single K-rich, seamount E-MORB (DR 28) has a distinctive pattern that cuts across those of the other axial ridge lavas (see section 5.2).

[28] The variability of the axial ridge lava population can be partially understood in terms of the covariation of La/Sm with La and MgO (Figure 17). In high-MgO (>7.5 wt.%) lavas of the axial ridge population (V–VII), La/Sm increases very steeply with decreasing MgO and increasing La. Together with the westward increase in La/Sm along the axial ridge region, this steep trend is consistent with simple mixing of a depleted (MORB) end-member with a relatively enriched end-member that is spatially related to the hot spot and apparently unrelated to the source of the DR 28 E-MORB. In more evolved lavas (MgO < 7.5 wt.%), La/Sm remains high but changes little with decreasing MgO. As in the MgO diagrams discussed in section 4.1, the axial ridge lavas become generally more evolved from east to west and these more evolved lavas appear to be derived from more enriched parents. La/Yb also increases east-west along the axial ridge domain, suggesting an increasing contribution from primary melts that have equilibrated with garnet and therefore formed to greater depth.

[29] The extended suite of trace elements represented in the spider diagrams of Figure 18 displays the same high variability for the axial ridge segments as described above for the rare earth elements. Of particular interest are the distinct negative anomalies in Sr concentration relative to the adjacent elements Pr and Nd. Both Sr concentrations and Sr anomalies display a number of systematic variations along the eastern GSC. (1) Sr concentrations change very little with decreasing MgO as a result of crystal fractionation (Figure 19a). (2) Sr concentrations are relatively constant within each segment, increasing slightly from Segment I–IV and more steeply from V–VII (Figure 19c). The east-west increase in Sr concentration from Segment V to Segment VII (Figure 19c) appears to correlate with decreasing MgO, defining an "over-enrichment" trend that is too steep to be accounted for by crystal fractionation alone. These observations require a

Table 3b. Rare Earth and Heavy Trace Element Analyses for Individual SO 158 Basalt Glasses[a]

Sample ID	Ba	La	Ce	Pr	Nd	Sm	Eu	Gd	Tb	Dy	Ho	Er	Tm	Yb	Lu	Hf	Ta	Pb[b]	Th	U
DR 3-1b	16.7	4.8	15.1	2.7	14.4	5.1	1.64	6.8	1.32	8.9	2.0	5.9	0.95	5.8	0.9	3.9	0.3	0.6	0.3	0.10
DR 6-2	23.1	8.1	25.1	4.3	22.2	7.3	1.99	9.3	1.80	12.1	2.6	7.9	1.27	7.7	1.2	6.3	0.5	0.6	0.6	0.20
DR10-2	16.5	3.7	11.5	2.1	10.9	3.9	1.30	5.2	1.02	6.9	1.5	4.5	0.73	4.5	0.7	2.9	0.3	0.5	0.3	0.09
DR13-4	17.7	3.5	10.6	1.9	10.0	3.6	1.30	5.0	0.98	6.6	1.5	4.5	0.72	4.4	0.7	2.6	0.3	0.5	0.2	0.07
DR14-1	24.8	4.1	11.7	2.0	10.3	3.6	1.29	4.7	0.94	6.3	1.4	4.1	0.66	4.0	0.6	2.6	0.3	0.5	0.3	0.10
DR16-1	25.4	5.0	14.4	2.5	12.9	4.4	1.51	5.8	1.12	7.5	1.7	5.0	0.79	4.8	0.7	3.3	0.4	0.6	0.4	0.13
DR17-2	30.5	6.0	17.2	2.9	14.5	4.9	1.67	6.3	1.23	8.1	1.8	5.3	0.84	5.1	0.8	3.7	0.5	0.7	0.5	0.16
DR17-21	23.5	4.2	12.3	2.4	11.0	3.7	1.34	5.0	0.96	6.4	1.4	4.2	0.66	4.0	0.6	2.8	0.3	0.5	0.3	0.10
DR18-1	32.0	5.5	15.6	3.0	13.6	4.6	1.62	6.0	1.15	7.6	1.6	4.9	0.77	4.8	0.7	3.4	0.5	0.7	0.4	0.14
DR19-1	48.1	7.7	19.6	3.1	14.9	4.7	1.61	5.8	1.08	7.1	1.5	4.5	0.71	4.3	0.7	3.4	0.7	0.7	0.7	0.21
DR21-1	31.3	5.9	16.7	2.8	14.0	4.7	1.61	6.0	1.16	7.7	1.7	4.9	0.78	4.7	0.7	3.5	0.5	0.6	0.5	0.16
DR21-4	35.4	6.5	18.3	3.4	15.6	5.2	1.77	6.7	1.28	8.4	1.8	5.4	0.85	5.2	0.8	3.9	0.5	0.7	0.6	0.19
DR22-10	22.6	4.4	12.6	2.2	11.1	3.8	1.32	5.0	0.96	6.5	1.4	4.3	0.68	4.1	0.6	2.8	0.4	0.5	0.3	0.11
DR22-2	34.8	6.2	17.1	2.9	14.0	4.6	1.58	6.0	1.13	7.5	1.6	4.8	0.76	4.6	0.7	3.4	0.5	0.7	0.5	0.16
DR23-2	29.5	5.6	15.9	2.8	13.6	4.5	1.56	5.9	1.14	7.6	1.6	4.9	0.78	4.8	0.7	3.4	0.5	0.6	0.5	0.15
DR24-1	32.4	5.7	15.9	2.7	13.2	4.4	1.50	5.6	1.05	6.9	1.5	4.4	0.70	4.2	0.7	3.2	0.5	0.6	0.5	0.16
DR25a-1	14.8	3.3	10.3	1.9	9.7	3.4	1.23	4.5	0.87	5.7	1.3	3.7	0.59	3.6	0.6	2.5	0.2	0.5	0.2	0.07
DR26-2	20.6	3.8	10.9	1.9	9.5	3.2	1.18	4.2	0.81	5.4	1.2	3.5	0.55	3.3	0.5	2.4	0.3	0.5	0.3	0.11
DR27a-1	29.9	5.2	14.5	2.5	11.9	3.9	1.39	4.9	0.92	6.0	1.3	3.8	0.59	3.6	0.6	2.8	0.4	0.6	0.4	0.14
DR28[d]	215.9	20.3	43.8	5.8	24.3	5.4	1.81	4.8		5.1		2.8		2.5		4.1	2.2	1.8	2.2	0.6
DR29a-1	43.8	7.0	18.6	3.1	14.2	4.4	1.51	5.4	1.00	6.5	1.4	4.1	0.64	3.9	0.6	3.3	0.6	0.7	0.6	0.20
DR30-5	7.3	1.6	5.3	1.1	5.8	2.3	0.90	3.2	0.65	4.5	1.0	3.0	0.47	2.9	0.5	1.6	0.1	0.3	0.1	0.03
DR31-4	33.7	5.8	15.7	2.7	12.6	4.1	1.40	5.0	0.95	6.2	1.3	3.9	0.61	3.7	0.6	3.0	0.5	0.6	0.5	0.16
DR32-1	42.4	6.9	18.3	3.1	14.0	4.3	1.51	5.4	1.00	6.4	1.4	4.0	0.63	3.8	0.6	3.2	0.6	0.7	0.6	0.20
DR33-2	45.5	7.2	19.1	3.2	14.4	4.4	1.55	5.5	1.02	6.6	1.4	4.0	0.63	3.8	0.6	3.3	0.6	0.7	0.6	0.21
DR34-11	56.8	9.1	23.5	3.9	17.3	5.2	1.81	6.3	1.12	7.2	1.5	4.4	0.67	4.0	0.6	3.9	0.8	0.8	0.8	0.25
DR34-3	56.4	8.9	23.2	3.9	17.3	5.2	1.78	6.2	1.13	7.2	1.5	4.4	0.68	4.0	0.6	3.9	0.8	0.9	0.8	0.26
DR35-1	115.7	20.1	50.0	8.1	35.3	10.1	2.99	12.0	2.14	13.5	2.8	8.3	1.31	7.8	1.2	8.0	1.8	1.4	2.0	0.60
DR36-2	180.4	34.9	83.9	13.6	56.4	15.5	4.16	17.7	3.09	19.5	4.0	11.9	1.87	11.3	1.7	12.7	3.2	1.7	3.8	1.10
DR36-4	185.1	36.1	86.9	14.7	58.8	16.1	4.29	18.4	3.23	20.3	4.2	12.2	1.91	11.6	1.8	13.2	3.2	1.7	4.0	1.15
DR36-5	175.7	34.3	83.4	13.5	56.3	15.3	4.13	17.6	3.07	19.2	4.0	11.7	1.84	11.1	1.7	12.6	3.1	1.7	3.7	1.09
DR37-1	34.0	5.5	14.9	2.6	12.1	3.9	1.42	4.8	0.89	5.7	1.2	3.5	0.53	3.2	0.5	2.8	0.5	0.6	0.4	0.14
DR38-1	76.2	11.7	29.6	4.9	21.1	6.1	2.06	7.3	1.30	8.2	1.7	5.0	0.77	4.6	0.7	4.5	1.1	1.1	1.1	0.35
DR43-1	6.5	1.3	4.3	0.9	4.9	2.0	0.79	3.0	0.62	4.4	1.0	3.0	0.48	3.0	0.5	1.4	0.1	0.3	0.0	0.03
DR43-2	6.5	1.3	4.3	0.9	4.9	2.0	0.79	3.0	0.62	4.4	1.0	3.0	0.48	3.0	0.5	1.4	0.1	0.3	0.0	0.03
DR48-1	59.5	7.1	18.2	3.1	13.7	4.3	1.51	5.3	0.98	6.4	1.3	4.0	0.62	3.8	0.6	3.1	0.7	0.7	0.7	0.20
DR48-4	40.2	5.4	14.6	2.6	12.0	3.9	1.42	4.9	0.92	5.9	1.2	3.7	0.57	3.4	0.5	2.9	0.5	0.6	0.4	0.14
DR49-1	113.0	12.6	31.1	5.2	21.8	6.4	2.10	7.7	1.39	9.0	1.9	5.6	0.87	5.3	0.8	4.9	1.2	1.1	1.3	0.37
DR49-2	151.4	17.4	42.3	7.2	29.1	8.3	2.53	9.9	1.76	11.2	2.3	6.9	1.08	6.6	1.0	6.5	1.7	1.4	1.8	0.53
DR49-4	102.9	11.7	28.8	4.8	20.1	5.8	1.96	6.9	1.23	7.8	1.6	4.8	0.74	4.5	0.7	4.3	1.1	1.1	1.2	0.34
DR53-1	115.8	11.0	26.4	4.4	17.7	5.0	1.66	6.1	1.11	7.1	1.5	4.5	0.70	4.3	0.7	3.8	1.2	0.9	1.2	0.34
DR53-3	85.3	8.1	19.5	3.2	13.4	3.9	1.40	4.8	0.89	5.7	1.2	3.6	0.56	3.4	0.5	2.9	0.8	0.8	0.8	0.23
DR54-1	43.8	5.0	12.8	2.3	9.9	3.3	1.22	4.2	0.79	5.2	1.1	3.3	0.52	3.1	0.5	2.3	0.5	0.6	0.5	0.14

Table 3b. (continued)

Sample ID	Ba	La	Ce	Pr	Nd	Sm	Eu	Gd	Tb	Dy	Ho	Er	Tm	Yb	Lu	Hf	Ta	Pb[b]	Th	U
K1919 average of 5 repeats[c]	138.6	16.2	40.5	6.4	26.6	6.5	2.2	6.6	1.0	5.6	1.0	2.7	0.4	2.1	0.3	4.7	1.5	1.3	1.2	0.4
StDev	2.6	0.3	0.7	0.4	0.5	0.1	0.0	0.1	0.0	0.1	0.0	0.1	0.0	0.0	0.0	0.1	0.0	0.0	0.0	0.0
BHVO accepted[d]	139	15.8	39	5.7	25.2	6.2	2.06	6.4	0.96	5.2	0.99	2.4	0.33	2.02	0.29	4.38	1.23	2.6	1.08	0.42

[a] All values in ppm. Solution ICP-MS analyses by Chris Russo in the W.M. Keck Collaboratory for Plasma Spectrometry at Oregon State University (http://wmkeck-icpms.coas.oregonstate.edu/).
[b] Pb data may be unreliable as replication of values for some rock standards is very poor. Nevertheless, unknown glass data plot correctly in normalized (spider) plots.
[c] Average of 5 replicates, run with samples, of rock standard K1919, equivalent to USGS standard BHVO-1.
[d] *Govindaraju* [1994] accepted values for BHVO-1.

general east-west increase in parental Sr contents, including a much steeper increase within the axial ridge domain. (3) Although Sr concentration changes very little with decreasing MgO, the magnitude of the Sr anomaly ($Sr^* = (Pr + Nd)_N/2 - Sr_N$) increases significantly as concentrations of the more incompatible adjacent rare earth elements increase (Figure 19b). Because of this fractionation enhancement, which implies buffering of Sr by plagioclase in the evolving magmatic liquids, Sr anomaly amplitudes actually increase with increasing proximity to the hot spot (Figure 19d). (4) Fractionation enhancement is not, however, the sole cause of the Sr anomalies as there is a significant range of Sr* values at any given MgO content, and even the most magnesian lavas from the eastern GSC have well-developed Sr anomalies. (5) If fractionation effects are eliminated by considering only the most primitive lavas, parental Sr anomaly magnitudes actually decrease toward the Galápagos hot spot (Figure 19), even as parental Sr concentrations increase.

[30] The persistence of the Sr anomalies in eastern GSC parental magmas, together with their westward decreasing amplitude, is consistent with progressive mixing between a Sr-poor, depleted primitive magma type, that is dominant in the eastern segments, and an enriched magma type, that is associated with the hot spot. The gradation in Sr* values suggest that this mixing is between magmas and not source materials and therefore that depleted melts in equilibrium with plagioclase-bearing mantle are present beneath most or all of the eastern GSC. Alternate models involving dynamic equilibrium between migrating melts and mantle or crustal plagioclase may also be possible, although the development of the strongest Sr anomalies in the most depleted primitive magmas seems inconsistent with any progressive/dynamic process. Recently, for example, *Saal and Van Orman* [2004] showed that diffusive interaction between percolating melts and a plagioclase-rich lower crust should lead to ^{226}Ra excesses in depleted MORB lavas. However, unpublished data of Kokfelt et al. (submitted manuscript, 2004) indicate a complete absence of excess ^{226}Ra in eastern GSC lavas, apparently precluding this particular model.

[31] In summary, the high variability of the axial ridge lava population and the systematic along-axis changes in Sr and Sr* seem to imply that at least two parental magma types are able to retain discrete identities in the uppermost mantle and may even remain separate as they traverse the subaxial magma

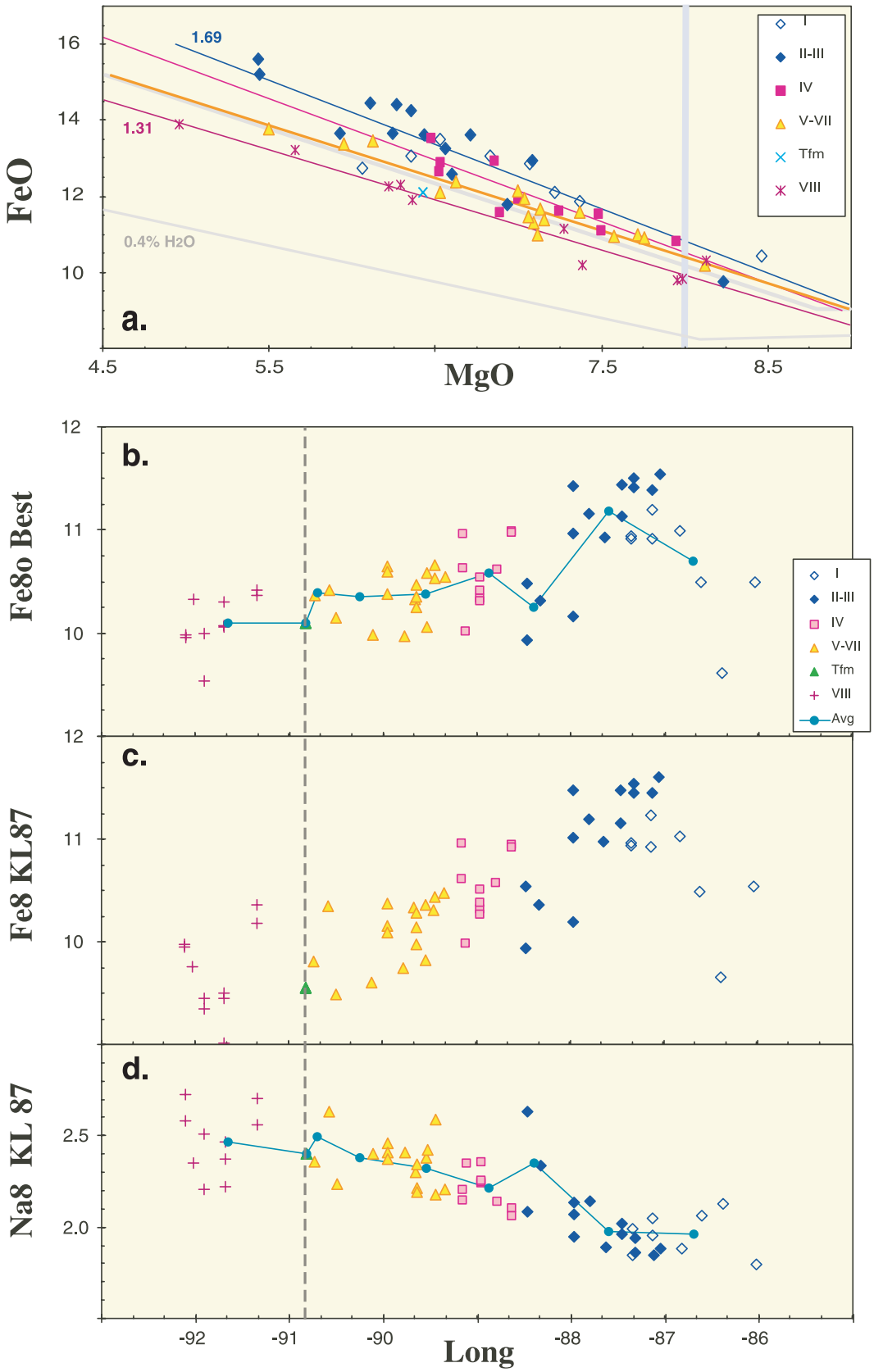
a.
FeO
MgO
1.69
1.31
0.4% H2O
I
II-III
IV
V-VII
Tfm
VIII
b.
Fe8o Best
c.
Fe8 KL87
d.
Na8 KL 87
Long
Avg

Figure 15

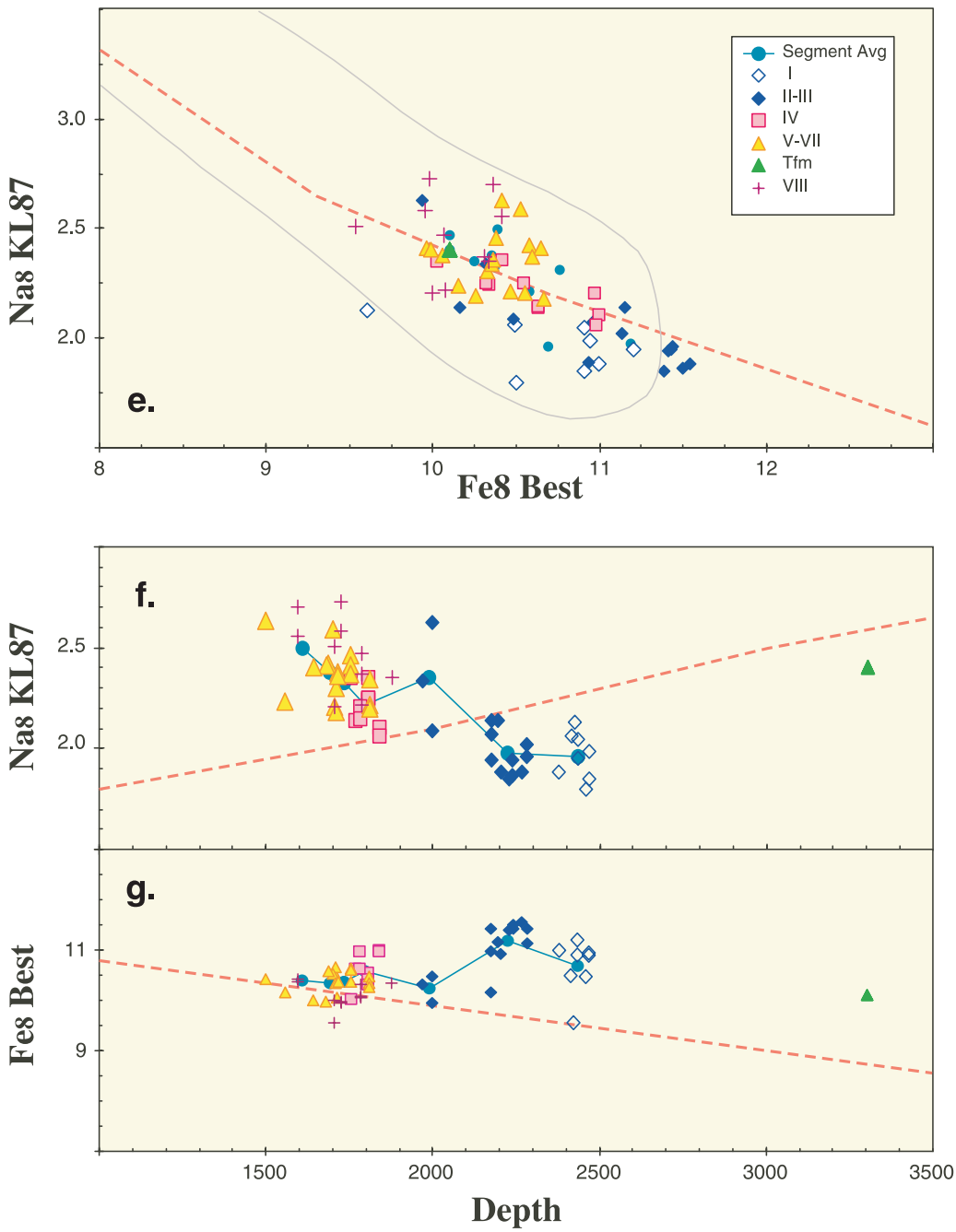

Figure 15. Figures illustrating the Na_8 and Fe_8 systematics of SO 158 basaltic glasses. Legend as for Figure 12. See text for discussion. (a) FeO-MgO variation diagram showing the progressive east-west shallowing of linear, least squares best fit LLDs, shown in color to match the symbols to which they are fitted. Numbers in figure are (absolute) slopes of the two outer LLDs. Thick and thin gray lines are dry and 0.4% H_2O model fractionation paths, respectively, from *Asimow and Langmuir* [2003]. (b) Along-axis variations in Fe_8, calculated using best fit LLD slopes from Figure 15a. Green line connects averages for each segment shown as green circles. (c and d) Along-axis variations in Fe_8 and Na_8, calculated using "standard" slopes from *Klein and Langmuir* [1987] (KL). (e) Na_8 versus Fe_8 for individual SO 158 basaltic glasses and morphological segment averages from the eastern GSC only. Fe_8 best fit values as in Figure 15b. Na_8 values as in Figure 15d. Longer (pink) line is the best fit global array of *Asimow and Langmuir* [2003]. Shorter (blue) line is best fit through all GSCeast basaltic glasses. Outlined field is the global array from *Langmuir et al.* [1992]. (f and g) Variations in Fe_8 (calculated from best fit LLDS) and Na_8 (KL LLDs) with axial depth. Reference line is the global array of *Klein and Langmuir* [1987].

systems and erupt in close proximity to one another. Further, magmas derived from the enriched end-member undergo varying, and often substantial, amounts of crystal fractionation while those from the more primitive end-member do not.

4.3. Regional Variations in Na_8 and Fe_8

[32] Calculations of Na_8, Fe_8, and similar "normalized" parameters are primarily intended to facilitate comparisons of primary or parental magma compositions within or between suites of MORB lavas. The normalizing calculation diminishes the contribution of postmelting magmatic processes, particularly crystal fractionation, to overall geochemical variability. The success of such calculations, and the level at which they are meaningful, depend critically on the purpose for which they are made, on the details of the calculation, and especially on the assumption of an appropriate liquid line of descent (LLD) with respect to MgO. *Klein and Langmuir* [1987] studied global variability using simple normalizing equations that assume linear variation with a constant, "global average" slope for FeO and Na_2O over a limited MgO range (8–6 wt.%). The majority of subsequent authors have followed this simple approach, while others have used regionally or geochemically variable slopes [e.g., *Plank and Langmuir*, 1988] or extrapolations based on higher order curves fit to the data in hand [e.g., *Douglas-Priebe*, 1998; *Cushman et al.*, 2004]. For "local" problems, there may be significant misfits between normalizations based on global average data and those based on local data.

[33] The eastern GSC provides an excellent example of a situation in which the details of the calculation can significantly affect the conclusions. For the small GSC data set available at the time, *Klein and Langmuir* [1987] and *Langmuir et al.* [1992] showed that Fe_8 (calculated using their global average LLD slope) decreases to a minimum near 92°W while Na_8 values increase. These "anomalous" depth relationships are opposite to those observed along the global mid-ocean ridge system and have become widely accepted as characteristic of many hot spot-influenced spreading centers. Here, for our larger data set, we compare the *Klein and Langmuir* [1987] (KL) global average slopes with segment-by-segment, linear best fit, "local" LLD slopes.

[34] For Na_2O, the local LLD slopes are not significantly different from the KL global average, and the along-axis Na_8 variation is the same by either method. For FeO, however, the picture is more complex. Best fit, linear FeO-MgO LLDs are steeper for the valley-and-ridge Segments I–III than for the axial ridge Segments V–VII (Figure 15a) and this has the effect of reducing the overall range of Fe_8 values relative to the range calculated for the single KL LLD slope. Because the LLD slope for Segments I–III is close to the KL value, the global KL Fe_8 values for Segments V–VII are lower than the "local" Fe_8 values (Figure 15c). Using the local Fe_8 values (Figure 15b), we can recognize three important characteristics of the eastern GSC lavas that are not apparent from the KL global calculation. First, there is an anomalous high-Fe_8 region between 86°50′W and 87°58′W (discussed further below) and second, when this high-Fe_8 region is excluded, Fe_8 is invariant with distance along-axis. The significance of these differences for our understanding of GSC magma genesis is discussed in section 5.3. A third observation is that Fe_8 values for segments V–VII appear normal for their axial depth, relative to the KL global depth correlation.

[35] The anomalous high-Fe_8 region encompasses the three subsegments that bound the 87°W OSC, but its origin and its relationship to the OSC are unclear. It includes both subsegments of Segment II and the western subsegment of Segment I. Each of these subsegments is characterized by a small but distinct axial ridge within the regional valley-and-ridge terrain, suggesting that they may have been produced by a relatively recent period of magmatic activity. High-Fe_8 lavas are not accompanied by low-Fe_8 lavas, except in DR17, which is at the boundary of the high-Fe_8 region in the Segment II/III axial discontinuity, and all are relatively evolved (mg# 54–46). In principle, the development of high Fe_8 values along a discrete section of the GSC could originate in the mantle, either as a change in composition or as a change in the melt regime, or it could reflect a change in the LLD, leading to use of an inappropriate slope in the normalization calculation. Because trace element concentrations in the high-Fe_8 region are indistinguishable from other Segment I–III lavas, a change in mantle composition or melting conditions seems unlikely. To account for the observed Fe_8 anomaly magnitude would require a change in LLD slope from the best fit value of −1.69, to a value close to −2.0. On the basis of fractional crystallization models of *Langmuir et al.* [1992] this amount of steepening could be accomplished by an increase in pressure from 1 atm. to 6–8 Kb. Why such a change would

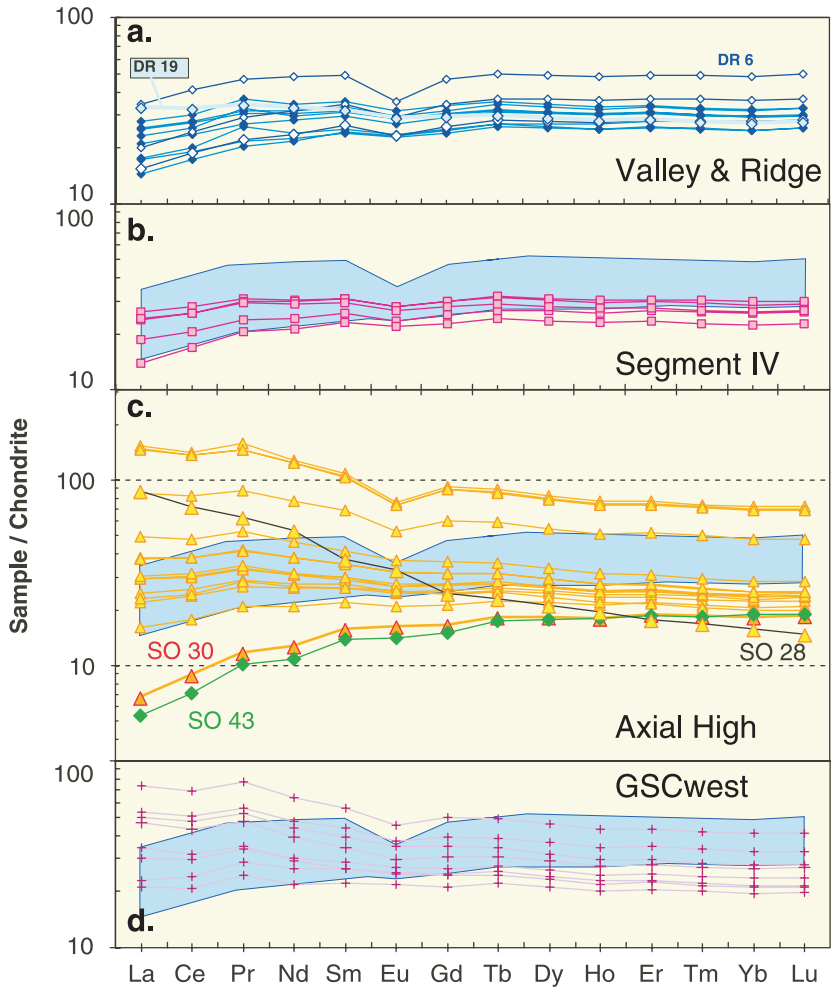

Figure 16. Chondrite normalized rare earth element diagrams for a representative subset of SO 158 glasses. Blue field in Figures 16b–16d encompasses the full range displayed in Figure 16a. (a) Glasses from the valley-and-ridge domain of Segments I–III. Note the crossing, relatively enriched pattern of DR 19 (broad light line) from the high-volume eruption in Segment III. DR 6 has higher values overall and a well-developed Eu anomaly. Both lavas are FeTi basalts that differ only slightly in major element composition from the remainder of the group. (b) Glasses from the transitional domain of Segment IV. (c) Glasses from the axial ridge domain display a remarkably diverse range of patterns and concentrations. Note the overall relative depletion in heavy REE and the progressive light REE enrichment as overall concentrations increase by differentiation. Lavas that plot above the blue field are highly differentiated andesites and FeTi basalts from Segment VI. Note the crossing, light REE enriched pattern (black line) of E-MORB lava SO 28 from the split seamount in Segment V and the near-identical, highly depleted patterns for basalt glasses SO 30 from the off-axis seamount in Segment V and SO 43 from the 91°W transform deep. (d) SO 158 glasses from the axial terrain of the western GSC between the Wolf-Darwin intersection and the 91°W transform display remarkably uniform patterns relative to those from the eastern axial ridge domain. Symbols as for Figure 12.

occur in the vicinity of the 87°W OSC remains unclear.

5. Constraints on Hot Spot–Spreading Center Interactions

5.1. Significance of Along-Axis Maxima

[36] The remarkable regional-scale, morphological, geochemical and geophysical symmetry around the Galápagos hot spot is similar in wavelength to other oceanic hot spots including Iceland, Hawaii, and Cape Verde [e.g., *Schilling*, 1991; *Ito and Lin*, 1995a; *Ito et al.*, 1997], and, at this scale, a wide variety of parameters display maxima (or minima) in the vicinity of 91°–92°W. These patterns are presumed to reflect regionally symmetrical, thermal and/or material inputs from the Galápagos mantle plume to the mantle beneath the spreading center. Superimposed on this apparently simple

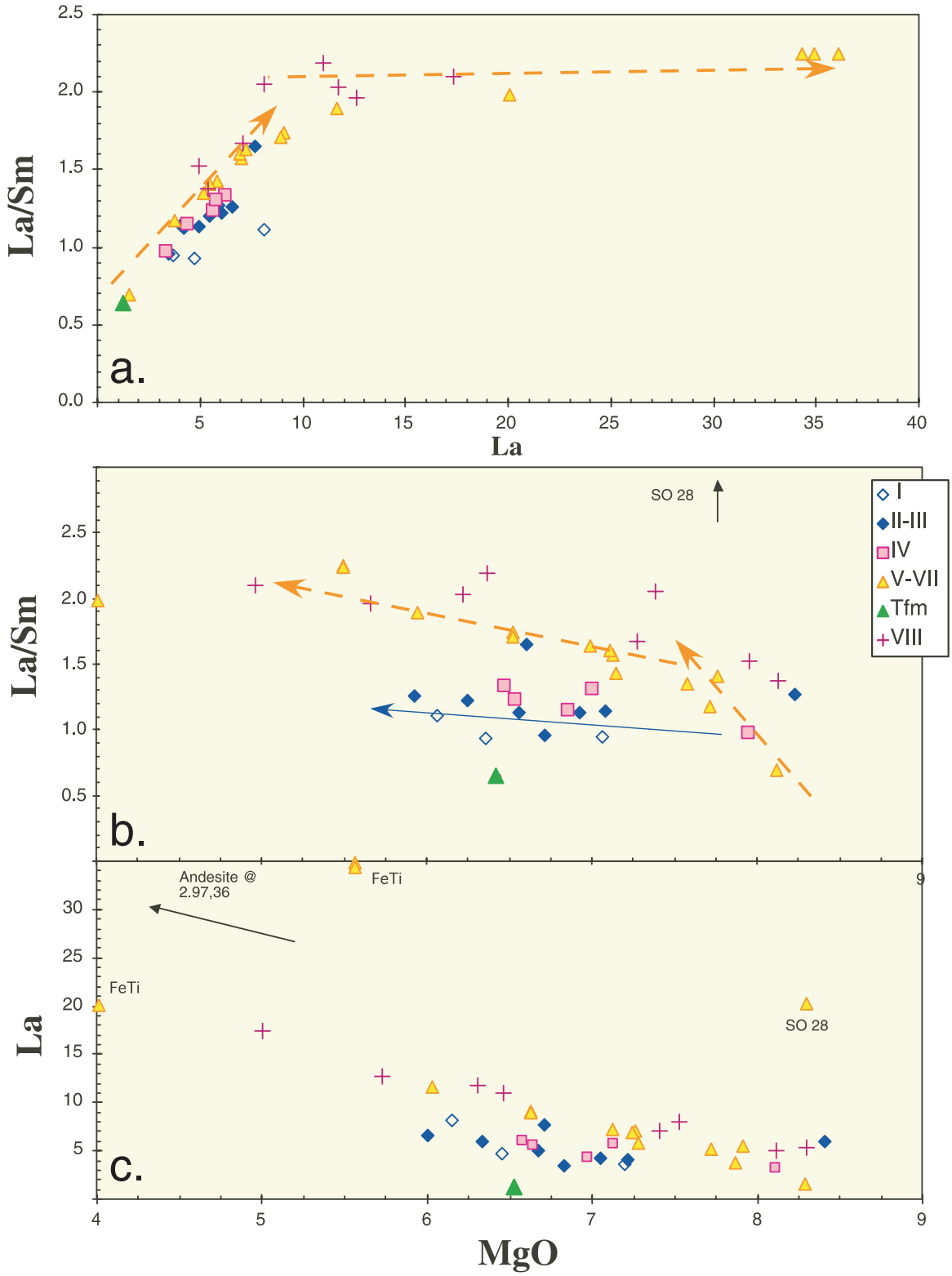

Figure 17. Figures illustrating the contrasting systematics of the valley-and-ridge (diamonds) and axial ridge (triangles) domains. La/Sm increases very rapidly with decreasing MgO for primitive axial ridge basaltic lavas (high MgO, low La), reflecting an increasing contribution from an enriched, plume-related source, while the more evolved axial ridge lavas appear to be derived by crystal fractionation only from relatively enriched parents. Basalts from the valley-and-ridge domain display a normal crystal fractionation trend derived from less enriched parents. Symbols as for Figure 12.

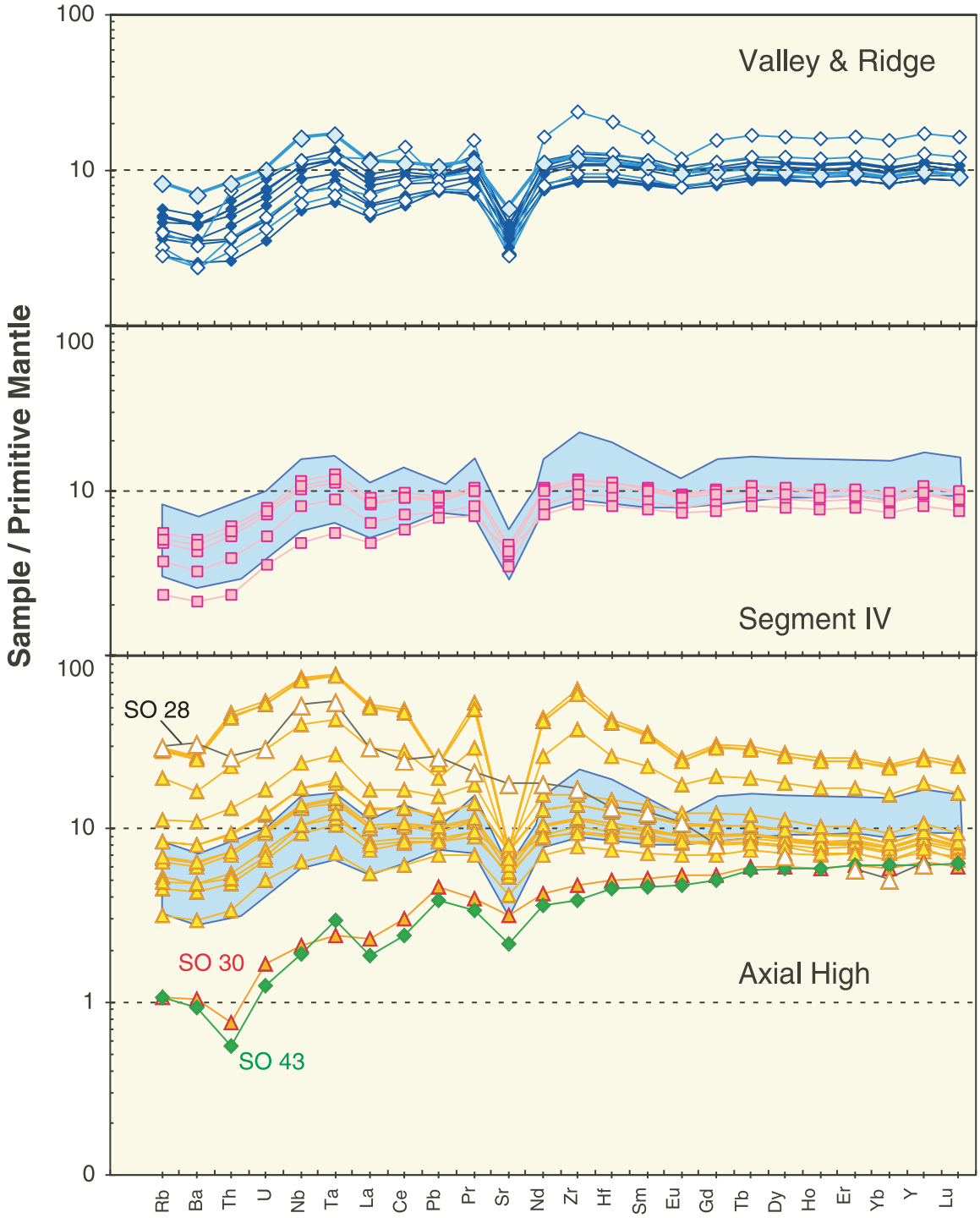

Figure 18. Spider diagrams normalized to primitive mantle of *Sun and McDonough* [1989] for a representative subset of SO 158 glasses. Blue field in lower panels encompasses all the data represented in the uppermost panel. Note the very high diversity of the axial ridge population and the progressive increase in negative Sr anomaly with increasing differentiation. Note the crossing pattern for E-MORB SO 28 and the highly depleted patterns of the off-axis seamount and transform lavas, SO 30 and SO 43. Symbols as for Figure 12.

regional pattern is a complex, segment-scale variability; individual parameters may vary in distinctly different ways and peak positions may vary from element-to-element or ratio-to-ratio. Variations in peak position were first noted for ratios of Sr and Nd isotopes and some trace elements [*Schilling et al.*, 1982, 2003; *Verma et al.*, 1983], although more recently, *Schilling et*

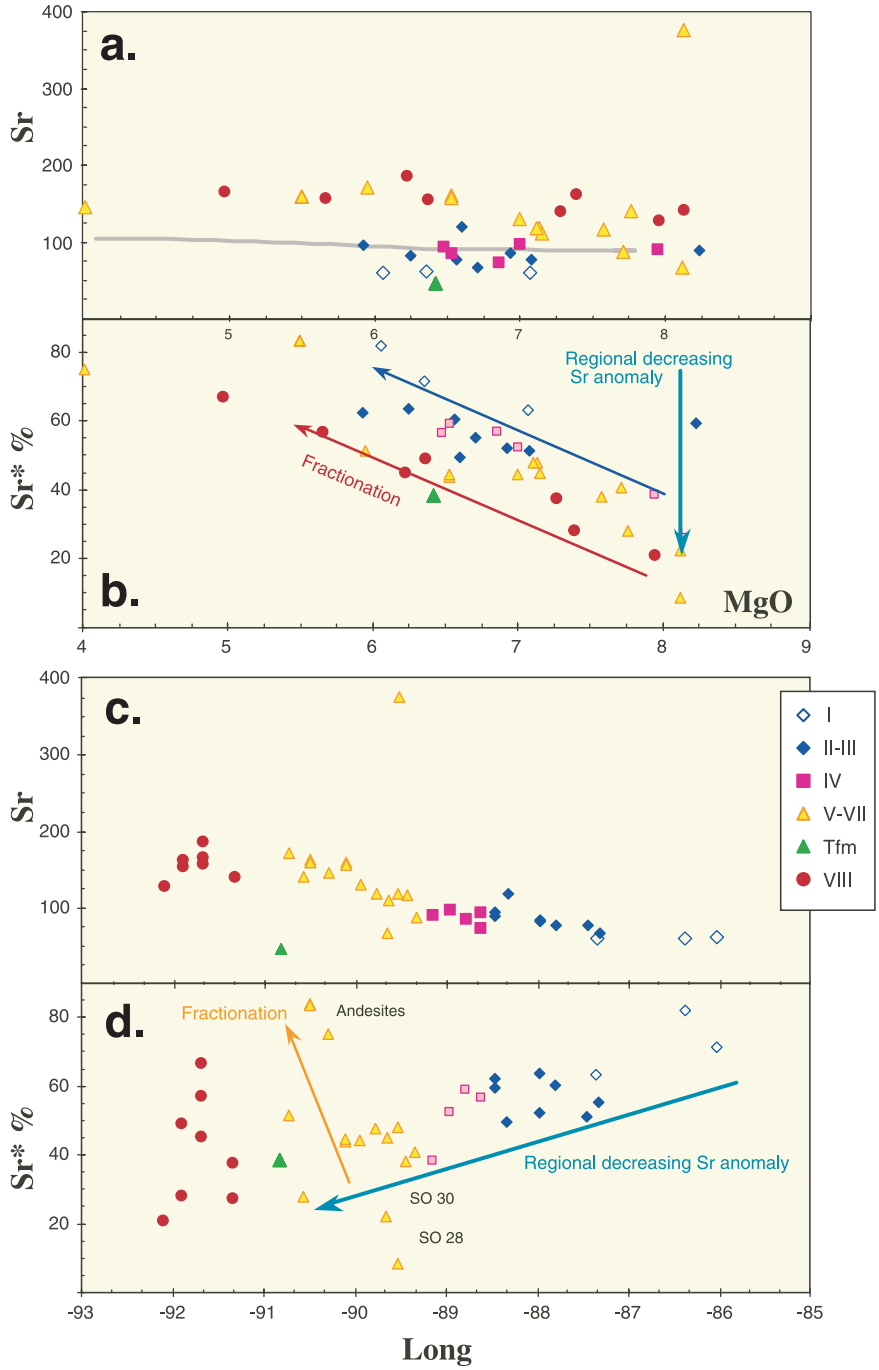

Figure 19. Figures illustrating the systematics of Sr and the Sr anomaly ($Sr^* = (Pr_N + Nd_N)/2 - Sr$). Sr* is calculated in mantle-normalized units and is expressed as a percentage of $(Pr_N + Nd_N)/2$). Sr* anomaly amplitude increases as a result of crystal fractionation, but the minimum anomaly amplitude and the anomaly amplitude in least-fractionated basalts both decrease toward the hot spot. See section 4.2 for a more detailed discussion.

al. [2003] discussed along-axis variations with reference to an assumed single point of symmetry at 91°30′W. Here we show that there are two principal peak locations and that, for a wide range of parameters, maxima (or minima) may occur in either or both locations.

[37] For isotopic ratios, we used the regional isotopic data set of *Schilling et al.* [2003] to ensure uniform coverage of the eastern and western GSC, as full isotopic coverage is not yet available for the newer sample sets. Using a simple, empirical linear regression technique, we were able to define a

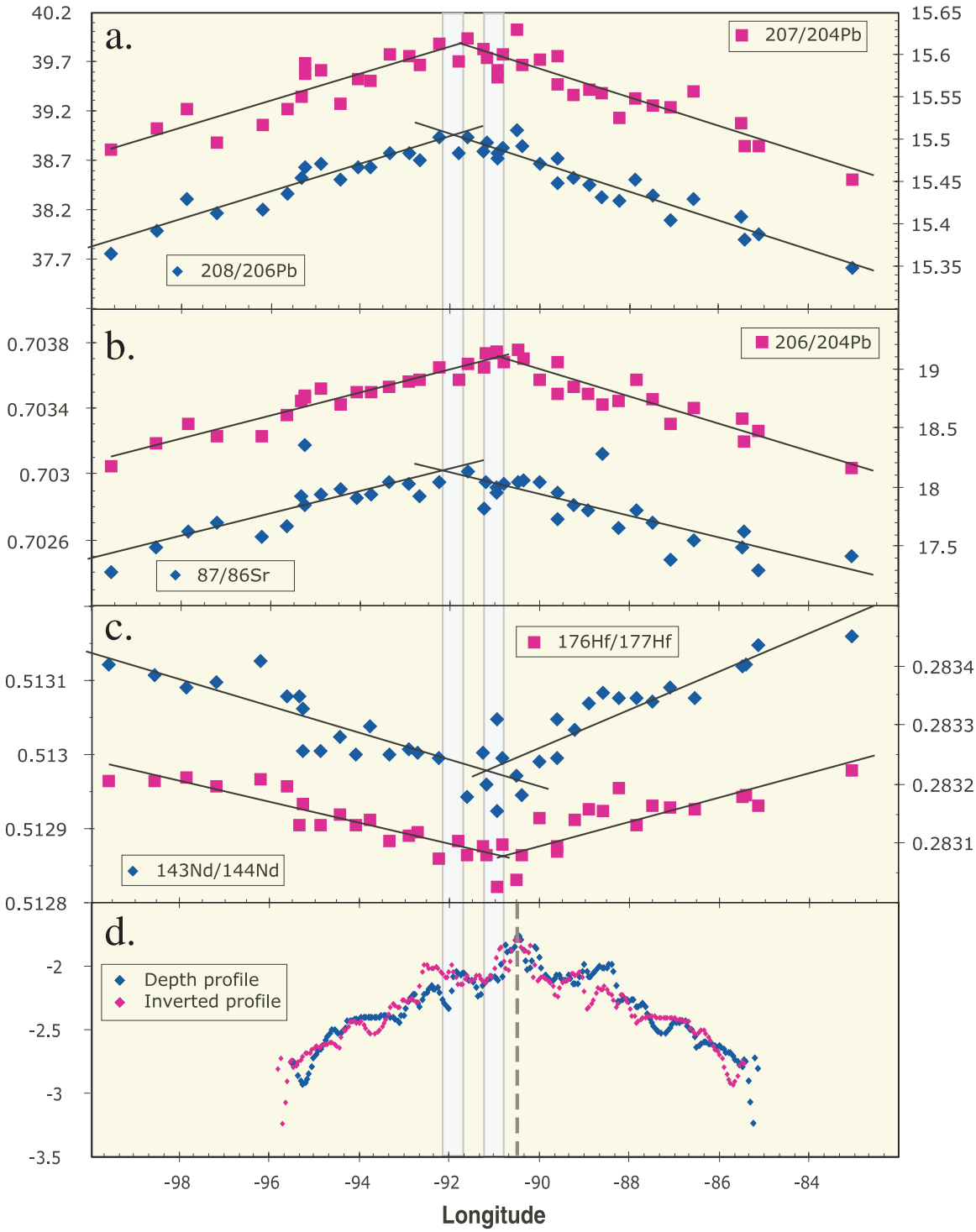

Figure 20

unique point of symmetry for each along-axis isotopic ratio profile. For each ratio in turn, we identified, by trial and error, the longitude at which the data divide into eastern and western populations, such that the eastern and western linear regression best fit lines intersect at the boundary longitude (Figure 20). For $^{87}Sr/^{86}Sr$, $^{207}Pb/^{204}Pb$, and $^{208}Pb/^{204}Pb$, the maxima coincide within 50 km, between 91°40′W and 92°10′W, while the $^{206}Pb/^{204}Pb$ maximum and the $^{143}Nd/^{144}Nd$ and $^{176}Hf/^{177}Hf$ minima fall between 90°45′W and 91°15′W. The western peak coincides with a local

topographic high, with an oblique line of small seamounts to the south of the GSC axis [*Sinton et al.*, 2003], and with peaks in a wide range of other geochemical parameters [*Cushman et al.*, 2004]. The eastern peak defined by the regression lines coincides with the 91°W transform and the closest approach of the GSC to the presumed hot spot location beneath the western Galápagos Islands. This peak lies to the west of the ~90°30′W peak defined by the trace element profiles (see section 4.1), but for those isotopic ratios that define the eastern peak, values remain well above the regression line for all locations across the trace element peak. A more precise evaluation of the relationships of the isotopic and elemental peaks to one another and to morphologic or other features, especially the 90°30′W calderas, will emerge as the isotopic analyses of our SO 158 samples become available.

[38] Axial depth variations along the GSC have previously been described by *Ito and Lin* [1995a] and *Schilling et al.* [1982, 2003]. *Ito and Lin* [1995a] used calculated isostatic depth profiles and concluded that these depths are symmetrical about the 91°W transform. *Schilling et al.* [2003] artificially divided the same depth data at their assumed point of symmetry (91°30′W) and concluded that the GSC to the east of this point is systematically shallower than the GSC to the west. They interpreted this observation as resulting from a contrast in thermal state reflecting the closer proximity of the eastern GSC to the hot spot. We used a simple visual technique to match the along-axis depth profile and its mirror image (Figure 20d). This method reveals a surprising mirror symmetry centered near the 90°30′W calderas, and therefore coincident with the eastern elemental peak.

[39] The double-peaked distribution of key mantle-source indicators is a fundamental new observation, strongly suggesting that there are two key loci for material transfer from the Galápagos plume to the GSC and that a different component of the plume is dominant at each locus. (The nature of the Galápagos plume components has been documented by *White et al.* [1993]; *Graham et al.* [1993]; *Hoernle et al.*, 2000; *Harpp and White* [2001]; *Blichert-Toft and White* [2001]; and *Harpp et al.* [2002]). On the basis of new Sr-Nd-Pb isotope data (F. Hauff et al., personal communication, 2004) and a combined trace element and U-series study (Kokfelt et al., submitted manuscript, 2004) of our new sample set, plume input near ~92°W is dominated by the "Northern" or "WD" component while, between the 91°W transform and the 90°35′W calderas, plume input is dominated by the "Central" or "PLUME" component. (Components defined by *Hoernle et al.* [2000] and *Harpp and White* [2001], respectively).

5.2. Near-Axis Seamounts and Other Transient Anomalies

[40] Lavas from two small, near-axis seamounts near ~88°30′W are distinct from those of the axial populations. Dredge DR 28 is from a recently split, near-axis seamount that straddles the axis at 89°31′W (Figure 8). DR 28 lavas appear to be unique among eastern GSC E-MORB in their high K_2O and K/Ti values and in their distinct rare earth patterns (see section 4.2). A nearby dredge (DR 29a) from the adjacent spreading axis yielded only N-MORB. The DR 28 E-MORB have markedly higher incompatible element concentrations and ratios (La/Sm(n) = 2.33, K_2O/TiO_2 = 0.42) and are significantly more enriched in terms of the elements discussed here than any other eastern

Figure 20. Regional variation in isotopic ratios over almost 1,500 km along the GSC using data of *Schilling et al.* [2003]. (a–c) For each of six well-measured isotopic ratios in turn, data are divided by longitude into eastern and western populations, such that the eastern and western least squares linear regression lines intersect at a common value, at the point where the populations are divided. This procedure reveals a strong mirror symmetry about the longitude of the division. The points of symmetry for $^{87}Sr/^{86}Sr$, $^{207}Pb/^{204}Pb$, and $^{208}Pb/^{204}Pb$ coincide within 50 km between 91°40′W and 92°10′W, while those for $^{206}Pb/^{204}Pb$, $^{143}Nd/^{144}Nd$, and $^{176}Hf/^{177}Hf$ coincide in a different band 90°45′W to 91°15′W. We interpret these "geochemical peaks" as points of maximum input to the GSC melting regime for two distinct, plume-related mantle components. For all ratios except Nd, the method is remarkably sensitive to latitude changes much smaller than the peak separation. (d) Isostatic axial depth profile (empirically projected from ridge flanks to eliminate dynamic topography at the axis) from *Ito et al.* [1997] is symmetrical about ~90°25′W. Symmetry is determined by finding the best visual match between the actual profile and its inverted mirror image. Here the actual profile is shown in dark blue, and the inverted profile is shown in pale red. A mismatch appears between 88°–89°W and 92°–93°W because sharp drops in the depth profiles reflect the axial ridge to valley-and-ridge transition. These drops are artifacts of the method of depth determination. Other mismatches primarily occur at segment boundaries. This method of determining symmetry is surprisingly sensitive. Significant flank-to-flank mismatches become apparent with shifts in the point of symmetry as small as 15 min.

GSC basalt and, indeed, than most or all western GSC basalts (Figure 12 and 14). The association of this unusual E-MORB occurrence with the transient increase in magma supply that formed the seamount at the spreading axis presumably reflects the passage of a discrete compositional heterogeneity through the melting region.

[41] A second type of young seamount lies 15 km south of Segment V at 89°39.7′W (Figure 8). It has a summit caldera, suggesting that it has been active in an off-axis setting, although its strong asymmetry, with a steep flank away from the GSC, may suggest that it formed close to the GSC in the region of active faulting. Basalts from a single dredge (DR 30) on this seamount are more highly depleted than all eastern GSC axial basalts (La/Sm(n) = 0.43, K_2O/TiO_2 = 0.04), except for DR 43 (Figures 12, 16, and 18), which is from the 91°W transform (Figure 11). Similar lavas have been reported from a number of seamounts in the northern and northeastern regions of the Galápagos Platform [*Harpp and White*, 2001; *Harpp and Geist*, 2002; *Harpp et al.*, 2002]. These occurrences suggest that an unusually depleted mantle component previously inferred beneath the northeast and eastern Galápagos Platform is also present beneath the eastern GSC, although not normally manifested in axial lavas.

[42] A small, localized apparent melting anomaly occurs near the center of Segment III at ~88°20′W, where a large (~30–40 km^2) lava flow or group of flows has buried the small-scale abyssal valley-and-ridge terrain (Figure 6). Lavas from DR 19 are N-MORB, but they are enriched relative to lavas of this and neighboring segments (but not to the eastern GSC overall) in incompatible trace element contents and ratios including Sr, K_2O/TiO_2, La/Sm, La/Yb, and Nb/Zr, but not Ba/Nb. The DR 19 flow appears to represent a recent, anomalously high volume eruption. The combination of relatively large eruption volume with a relatively enriched trace element signature again suggests the involvement of a small transient heterogeneity in the melt regime.

5.3. Na_8 and Fe_8: Hot Spot Influence, Global Trends, and Hydrous Melting

[43] The GSC is the type example of a hot spot-influenced ridge for which the global correlations among Na_8, Fe_8, and axial depth are distinct from those of the "global MORB array" [e.g., *Klein and Langmuir*, 1987, 1989; *Langmuir et al.*, 1992; *Asimow and Langmuir*, 2003]. Segment-averaged Na_8 values increase monotonically with decreasing depth from east to west, defining a trend that is "orthogonal" to the global array, such that axial ridge lavas have high Na_8, and valley-and-ridge lavas have low Na_8, relative to other spreading centers of similar depth (Figure 15f). Despite this departure from the global Na_8-axial depth array, eastern GSC lavas plot within the normal globalarray of decreasing Na_8 with increasing Fe_8 (Figure 15e), and only the high-Fe lavas plot significantly above the global Fe_8-depth array (Figure 15g).

[44] In principle, the ~1 wt.% increase in Na_8 approaching the hot spot could reflect an increase in bulk mantle Na-content, a decrease in mean extent of melting, or a combination of the two. *Langmuir et al.* [1992] showed that the maximum increase in Na_8 potentially attributable to mantle compositional variations is also about 1 wt.%, comparable to the observed range of values, but insufficient to fully offset the ~0.4 wt.% decrease that would be expected for the observed depth range, on the basis of the global array for constant mantle composition. Although simplistic, these figures suggest that some decrease in overall extent of melting must occur along the GSC, even as the overall melt production is increasing. Recently, *Detrick et al.* [2002], *Asimow and Langmuir* [2003], and *Cushman et al.* [2004] have shown that this apparent discrepancy is easily explained as an effect of the addition of H_2O from the Galápagos mantle plume. The presence of a mantle volatile phase leads to greatly increased depths of initial melting, creating an enlarged melt region below the dry solidus depth. An important, and counter-intuitive, consequence of this enlargement is that it allows the possibility of simultaneously increasing overall melt production while decreasing overall melt fraction. This process has been modeled for the western GSC by *Cushman et al.* [2004] and discussed in a broader context by *Asimow and Langmuir* [2003]. The westward increases in La/Yb and the overall lower heavy REE concentrations in axial ridge lavas are consistent with an abrupt transition to a deeper melt region.

[45] If hydrous melting is important beneath the eastern GSC, then it should have predictable and observable consequences for the subsequent evolution of basaltic magmas, consistent with those proposed by *Asimow and Langmuir* [2003]. Shallow crystallization of volatile-enriched magmas from hydrous melting regimes will give rise to

hydrous LLDs that are distinct from those of dry systems. As H_2O increases in the melt, the onset of plagioclase crystallization, and therefore of rapid FeO increase in the melt, is delayed to lower MgO values. Thus evolved lavas from hydrous regimes should have much lower FeO for a given MgO than those from dry systems. The magnitude of the expected difference is illustrated by the wet and dry LLDs in Figure 15a, and by abundant data from the Azores region shown in Figure 4 of *Asimow and Langmuir* [2003]. Accurate calculations of Fe_8 and other normalized parameters for such hydrous systems require much shallower LLD slopes than those for dry systems (consistent with discussion in section 4.3). Consequently, normalizations based on the steeper KL global LLD slopes will result in apparent Fe_8 values that are "too low." Similar arguments can be made for CaO and Al_2O_3. Removal of these elements from basaltic liquids by plagioclase crystallization is delayed in hydrous systems, resulting in enhanced apparent Ca_8 and Al_8 if global average normalizations are used. Enhanced apparent Ca_8 and Al_8 and decreased apparent Fe_8 were identified by *Asimow and Langmuir* [2003] as important indicators of hydrous melting.

[46] For the eastern GSC, the observed westward increases in CaO and Al_2O_3 and decreases in FeO (for any given MgO) are consistent in sense with an increasing role for deep hydrous melting, but the observed changes are small. For FeO (Figure 15a), the segment best fit LLD slopes decrease westward, but they are never as shallow as those for the hydrous models of *Asimow and Langmuir* [2003], or even clearly distinct from dry crystallization models. In fact, the only lavas from anywhere on the GSC that have low FeO relative to the dry FeO-MgO LLDs are most of the E-MORB from ~91°30′W to ~92°30′W, in the vicinity of the western geochemical peak [see *Cushman et al.*, 2004, Figure 6], three E-MORB analyzed by *Fisk et al.* [1982] and included in Figure 4b of *Asimow and Langmuir* [2003], and the seamount E-MORB, DR 28. Of these, only DR 28 and one *Fisk et al.* [1982] sample (T6-1) are from the eastern GSC, and these are from the same location (within ~5 km), presumably from the same small seamount.

[47] The scarcity of low-Fe lavas along the GSC, raises an important question. What is the along-axis extent of hydrous melting beneath the GSC? The restriction of low apparent Fe_8 values to a small section of the western GSC suggests that hydrous melting effects are dominant only beneath this small, shallow region. In this respect the GSC contrasts with the FAZAR region of the MAR, where abundant low-FeO lavas are associated with the more H_2O-rich melt regime associated with the Azores hot spot [*Asimow and Langmuir*, 2003]. For some other elements, especially K_2O, Na_2O, H_2O, and TiO_2, hydrous melting models [*Cushman et al.*, 2004] appear to explain key geochemical characteristics of GSC lavas. Na_8 systematics, in particular, suggest that hydrous melting effects extend beyond this narrow region to include part of the eastern GSC. If this is the case, then at least for Fe, Ca, and Al, LLDs of GSC magmas are not substantially affected by enhanced water contents. Finally, the general conformity of local Fe_8 values to the global depth array, especially in the axial ridge domain, appears to be inconsistent with the anomalously deep mean depths of melting implied by hydrous melting models. This implies either that Fe is relatively enriched in wet melts at high pressure, or, perhaps more likely, that bulk melt Fe contents are buffered by mantle-melt reactions within the dry melting region.

[48] A thorough evaluation of the role of water in melting and evolution of GSC magmas will require more detailed modeling of both melting and crystallization effects, consideration of a comprehensive suite of volatile analyses, and consideration of mantle source composition through isotopic analysis. Currently available evidence suggests, however, that melting and subsequent magmatic evolution in the vicinity of the western geochemical peak are dominated by hydration effects, with a rapid drop in normalized water contents to a background level of ~0.2 wt.%, away from the western geochemical peak [see *Cushman et al.*, 2004, Figure 6]. Elsewhere beneath the axial ridge terrains, the evidence for hydrous melting is more equivocal and segment-scale lava populations define LLDs that are effectively dry. Nevertheless, several lines of evidence, including the systematic variations in La/Sm, La/Yb, and Sr* discussed above, are consistent with limited inputs of mantle water causing deep initial melting, beneath the axial ridge terrains of the eastern GSC. Such observations have important implications for the details of material transfer from the Galápagos mantle plume to the GSC. If, as we have proposed, the eastern and western geochemical peaks are loci for transfer of discrete plume components, then the western component must have a significantly higher H_2O content. If this conclusion can be verified, it has important implications for the nature of plume-spreading center material transfer, and

potentially for the distribution of water among the plume components and for the nature of the plume itself.

6. Summary and Conclusions

[49] Multibeam bathymetric data collected during cruise SO 158 of R/V *Sonne* document the morphological evolution of the eastern GSC as it shallows westward toward its closest approach to the Galápagos hot spot, near the 91°W transform. As the spreading axis shallows, the dominant axial morphology evolves from a low-relief, valley-and-ridge domain to an increasingly prominent axial ridge domain. This evolution closely mirrors that of the western GSC and is consistent with increasing dominance of extrusive over tectonic processes as magma supply increases toward the hot spot. Seven morphological segments are separated by small axial discontinuities or offsets. The only large offset is the 87°W overlapping spreading center, which has a long (~2 m.y.) history of eastward propagation.

[50] The eastern GSC can be divided into two principal magmatic and morphologic domains, coinciding with the axial ridge and valley-and-ridge terrains (Segments V–VII and I–III, respectively), and separated by the transitional Segment IV. Each of the two principal magmatic segments spans three morphologic segments and each encompasses significant along axis geochemical variations, largely independent of axial offsets or volcano-tectonic morphology. The lava populations of the axial ridge Segments (V–VII) are characterized by complex magmatic histories that involve steep along-axis gradients in the more incompatible elements and ratios, contributions from a broad array of parental magma compositions and ''over-enrichments'' in some elements that appear to require the most fractionated lavas to be derived from the most enriched parental compositions. In contrast, the valley-and-ridge lava population of Segments I–III is predominantly controlled by shallow crystal fractionation processes with a relatively restricted array of parental magma compositions.

[51] The remarkable contrast between the high, source-related petrologic variability of the magmatically active axial ridge domain, and the fractionation-dominated, low petrologic variability of the magma deficient valley-and-ridge terrain is highly anomalous because it is in the opposite sense to that normally observed between axial ridge and axial valley mid-ocean spreading systems. We interpret this superposition of high intra-segment variability in a region of high magma production as reflecting a complex and variable array of material inputs from the Galápagos hot spot to the GSC. The expression of this complexity at the seafloor, and the development of ''over-enrichment'' trends, may be facilitated and/or enhanced by phenomena associated with channelized melt transport. Recent modeling by *Spiegelman and Kelemen* [2003] has shown that highly variable MORB populations can arise, even in the absence of a complex source, as melts become organized into channels that traverse the melt region. Within individual channels, more enriched melts, originating at greater depth, may occupy the center, while more depleted, and presumably cooler, melts occur close to the walls. Both types may be delivered as discrete entities to the ocean crust or even to the seafloor. We speculate that, as these coexisting melts begin to crystallize in the upper part of the channel system, the warmer, more enriched melts can remain partially molten for longer periods allowing for protracted crystal fractionation. Cooler, more depleted melts retain less heat; they are unable to remain molten for significant periods and hence are unlikely to become significantly fractionated. An additional factor may be that the cooler, more depleted melts are buffered by reaction with ambient shallow mantle throughout the melt region, reaching crustal depths with well-developed Sr depletions and primitive, high-MgO compositions, despite their lower temperatures.

[52] The GSC has become known as the type example of a hot spot-influenced ridge for which the global correlations among Na_8, Fe_8, and axial depth are anomalous relative to those of the ''global MORB array.'' Our new data confirm that the covariation of Na_8 with axial depth is anomalous and orthogonal to the global trend as first pointed out by *Klein and Langmuir* [1987]. Nevertheless, Na_8 retains a negative covariation with Fe_8 and values lie within the well-documented global array. The occurrence of high-Na_8 lavas at shallow axial depths close to the hot spot is consistent with emerging hydrous melting models that allow for lower overall melt fractions from a region of enhanced melt production. Fe_8 variations along the eastern GSC are complicated by segment-scale variations in the apparent liquid lines of descent (LLD) and by a region of anomalous high Fe_8 on either side of the 87°W OSC. Decreasing FeO-MgO LLD-slopes approaching the hot spot are consistent in sense with those predicted for the hydrous lavas

expected from a hydrous melting regime, but the decreases are much smaller than expected for significant melt H_2O contents. In addition, Fe_8 values from the axial ridge domain are "normal" for their axial depth. For the eastern GSC, then, Fe systematics do not appear to require either deep hydrous melting or subsequent melt evolution under hydrous conditions. Given that hydrous melting models appear to explain other key geochemical characteristics of GSC lavas [*Cushman et al.*, 2004], we conclude that the principal locus for transfer of water from the Galápagos plume to the GSC is localized between 91°30′W and 92°30′W, with a broader region, perhaps corresponding to the axial ridge terrains, in which mantle water contents are elevated but not to the level at which their effects are readily distinguishable.

[53] On a broader scale, regional linear gradients in isotopic ratios are highly symmetrical about either of two central geochemical peaks. The western geochemical peak, between 91°40′W and 92°10′W, is defined by $^{87}Sr/^{86}Sr$, $^{207}/^{204}Pb$, and $^{208}Pb/^{204}Pb$ and coincides with a local depth minimum and with an oblique line of small seamounts to the south of the GSC axis [*Sinton et al.*, 2003]. The eastern peak, although currently less clearly delineated, is defined by $^{206}Pb/^{204}Pb$, $^{143}Nd/^{144}Nd$ and $^{176}Hf/^{177}Hf$ and coincides with the closest approach of the GSC to the Galápagos Islands. It is manifested along the eastern GSC between the 91°W transform and two prominent calderas that surmount broad shield volcanoes near 90°35′W. Along-axis distributions of the more incompatible, source-dependent elements are also consistent with separate eastern and western peaks. Distinct differences, in key mantle-source indicators, between the geochemical peaks strongly suggest that there are two key loci for material transfer of different components from the Galápagos plume to the GSC.

[54] Taken together, our new data reinforce the established conclusion that thermal and material inputs from the Galápagos hot spot have a strong, symmetrical, long-wavelength influence on all aspects of spreading and crustal accretion for several hundred kilometers on either side of the Galápagos Islands. Our new data provide more detail, strongly suggesting that there are two key loci for material transfer from the Galápagos mantle plume to the GSC. Apparent inconsistencies in the complex interelement and along-axis relationships imply a complex interplay among: (1) multicomponent mantle-source compositions, (2) thermal and compositional (especially H_2O) perturbations in the parameters that control melting and magma evolution, (3) processes of magma segregation and transport, especially melt channelization, and (4) the complex present-day and historic geodynamic interplay between the Galápagos hot spot, the Cocos and Nazca plates, and the GSC.

Acknowledgments

[55] The ideas expressed here build upon many years of open exchange of ideas and data among those with interests in the Galápagos region. We thank (in random order) Dave Graham, Bob Duncan, Karen Harpp, Dennis Geist, Terry Naumann, Garrett Ito, John Sinton, Buffy Cushman, Pablo Canales, Bob Detrick, Bill White, Dan Fornari, and we especially apologize to anyone inadvertently omitted. We especially thank John Sinton and Dennis Geist and David Graham for thoughtful and thought-provoking reviews, Bill White for helpful comments, and Buffy Cushman and John Sinton for access to unpublished data and manuscripts. We sincerely thank the following people and entities without whom this work could not have happened: The Government of Ecuador for permission to work in its territorial waters. E. Santana for help in obtaining this permission and for assisting the science party during the expedition. The Master, crew, and Shipboard Scientific Party of R/V *Sonne* for their expert support during Expedition SO 158. Paul Wintersteller and Matthias Müller for help with processing of the bathymetric data. Chris Russo for performing the geochemical analyses with support from Adam Kent, Roger Nielsen, Ed Kohut, and Andy Ungerer. This study was supported by the German Ministry of Education and Research (BMBF; Grant MEGAPRINT). Participation by Christie and Hanan was supported by the U.S. National Science Foundation. Several figures were prepared with GMT public domain software [*Wessel and Smith*, 1995].

References

Ariskin, A. A., M. Y. Frenkel, G. S. Barmina, and R. L. Nielsen (1993), COMAGMAT: A Fortran program to model magma differentiation processes, *Comput. Geosci.*, *19*, 1155–1170.

Asimow, P. D., and C. H. Langmuir (2003), The importance of water to oceanic mantle melting regimes, *Nature*, *42*, 815–820.

Blichert-Toft, J., and W. M. White (2001), Hf isotope geochemistry of the Galapagos Islands, *Geochem. Geophys. Geosyst.*, *2*, doi:10.1029/2000GC000138.

Canales, J. P., J. J. Danobeitia, R. S. Detrick, E. E. Hooft, R. Bartolome, and D. F. Naar (1997), Variations in axial morphology along the Galápagos spreading center and the influence of the Galápagos hotspot, *J. Geophys. Res.*, *102*, 27,341–27,354.

Canales, J. P., G. Ito, R. S. Detrick, and J. M. Sinton (2002), Crustal thickness along the western Galápagos spreading center and the compensation of the Galápagos hotspot swell, *Earth. Planet. Sci. Lett.*, *203*, 311–327.

Christie, D. M., and J. M. Sinton (1981), Evolution of abyssal lavas along propagating segments of the Galápagos spreading center, *Earth Planet. Sci. Lett.*, *56*, 321–335.

Cushman, B., J. Sinton, G. Ito, and J. Eaby Dixon (2004), Glass compositions, plume-ridge interaction, and hydrous melting along the Galápagos Spreading Center, 90.5°W to 98°W, *Geochem. Geophys. Geosyst.*, *5*, Q08E17, doi:10.1029/2004GC000709.

Detrick, R. S., J. M. Sinton, G. Ito, J. P. Canales, M. Behn, T. Blacic, B. Cushman, J. E. Dixon, D. W. Graham, and J. J. Mahoney (2002), Correlated geophysical, geochemical, and volcanological manifestations of plume-ridge interaction along the Galápagos Spreading Center, *Geochem. Geophys. Geosyst.*, *3*(10), 8501, doi:10.1029/2002GC000350.

Douglas-Priebe, L. M. (1998), Geochemical and petrogenetic effects of the interaction of the Southeast Indian Ridge and the Amsterdam-Saint Paul hotspot, M.S. thesis, 132 pp., Oregon State Univ., Corvallis.

Duncan, R. A., and R. B. Hargraves (1984), Caribbean region in the mantle reference frame, in *The Caribbean-South American Plate Boundary and Regional Tectonics*, edited by W. Bonini et al., *Mem. Geol. Soc. Am.*, *162*, 89–121.

Embley, R. W., K. M. Murphy, and C. G. Fox (1990), High resolution studies of the summit of Axial volcano, *J. Geophys. Res.*, *95*, 12,785–12,812.

Fisk, M. R., A. E. Bence, and J.-G. Schilling (1982), Major element chemistry of Galápagos rift magmas and their phenocrysts, *Earth Planet. Sci. Lett.*, *61*, 171–189.

Fornari, D. J., M. R. Perfit, A. Malahoff, and R. W. Embley (1983), Geochemical studies of abyssal lavas recovered by DSRV Alvin from eastern Galápagos Rift, Inca Transform, and Ecuador Rift: 1. Major element variations in natural glasses and spatial distribution of lavas, *J. Geophys. Res.*, *88*, 10,519–10,529.

Geist, D. J. (1992), An appraisal of melting processes and the Galápagos Hotspot: Major- and trace-element evidence, *J. Volcanol. Geotherm. Res.*, *52*, 65–82.

Geist, D. J., W. M. White, and A. R. McBirney (1988), Plume-asthenosphere mixing beneath the Galápagos Archipelago, *Nature*, *333*, 657–660.

Geldmacher, J., B. B. Hanan, J. Blichert-Toft, K. Harpp, K. Hoernle, F. Hauff, R. Werner, and A. C. Kerr (2003), Hafnium isotopic variations in volcanic rocks from the Caribbean Large Igneous Province and Galápagos hot spot tracks, *Geochem. Geophys. Geosyst.*, *4*(7), 1062, doi:10.1029/2002GC000477.

Govindaraju, K. (1989), 1989 compilation of working values and sample description for 272 geostandards, *Geostand. Newsl.*, *13*, 1–113.

Govindaraju, K. (1994), 1994 Compilation of working values and description for 383 geostandards, *Geostand. Newsl.*, *18*, 1–158.

Graham, D. W., D. M. Christie, K. S. Harpp, and J. E. Lupton (1993), Mantle plume helium in submarine basalts from the Galápagos Platform, *Science*, *262*, 2023–2026.

Harpp, K. S. (1995), Magmatic evolution of mid-ocean ridges and hotspots: Isotopic and trace element studies of the East Pacific Rise, Mid-Atlantic Ridge, and Galápagos Islands, Ph.D. thesis, Cornell Univ., Ithaca, N. Y.

Harpp, K., and D. Geist (2002), Wolf-Darwin lineament and plume-ridge interaction in northern Galápagos, *Geochem. Geophys. Geosyst.*, *3*(11), 8504, doi:10.1029/2002GC000370.

Harpp, K. S., and W. M. White (2001), Tracing a mantle plume: Isotopic and trace element variations of Galápagos seamounts, *Geochem. Geophys. Geosyst.*, *2*, doi:10.1029/2000GC000137.

Harpp, K. S., K. R. Wirth, and D. J. Korich (2002), Northern Galápagos Province: Hotspot-induced, near-ridge volcanism at Genovesa Island, *Geology*, *30*(5), 399–402.

Hauff, F., K. Hoernle, H.-U. Schmincke, and R. Werner (1997), A mid Cretaceous origin for the Galápagos Hotspot: Volcanological, petrological, and geochemical evidence from Costa Rican oceanic crustal segments, *Geol. Rundsch.*, *86*, 141–155.

Hauff, F., K. Hoernle, P. van den Bogaard, G. Alvarado, and D. Garbe-Schönberg (2000a), Age and geochemistry of basaltic complexes in western Costa Rica: Contributions to the geotectonic evolution of Central America, *Geochem. Geophys. Geosyst.*, *1*, doi:10.1029/1999GC000020.

Hauff, F., K. Hoernle, G. Tilton, D. Graham, and A. C. Kerr (2000b), Large volume recycling of oceanic lithosphere over short time scales: Geochemical constraints from the Caribbean Large Igneous Province, *Earth Planet. Sci. Lett.*, *174*, 247–263.

Hey, R. N. (1977), Tectonic evolution of the Cocos-Nazca spreading center, *Geol. Soc. Am. Bull.*, *88*, 1404–1420.

Hey, R., G. L. Johnson, and A. Lowrie (1977), Recent plate motions in the Galápagos area, *Geol. Soc. Am. Bull.*, *88*, 1385–1403.

Hoernle, K. A., R. Werner, J. P. Morgan, D. Garbe-Schönberg, J. Bryce, and J. Mrazek (2000), Existence of complex spatial zonation in the Galápagos plume for at least 14 m. y., *Geology*, *28*, 435–438.

Hoernle, K. A., F. Hauff, and P. van den Bogaard (2004), A 70 Myr history (69–139 Ma) for the Caribbean Large Igneous Province, *Geology*, in press.

Ito, G., and J. Lin (1995a), Mantle temperature anomalies along the present and paleoaxes of the Galápagos spreading center as inferred from gravity analyses, *J. Geophys. Res.*, *100*, 3733–3745.

Ito, G., and J. Lin (1995b), Oceanic spreading center-hotspot interactions: Constraints from along-isochron bathymetric and gravity anomalies, *Geology*, *23*, 657–660.

Ito, G., J. Lin, and C. W. Gable (1997), Interaction of mantle plumes and migrating mid-ocean ridges: Implications for the Galápagos plume-ridge system, *J. Geophys. Res.*, *102*, 15,403–15,417.

Kellogg, J. N., and V. Vega (1995), Tectonic development of Panamá, Costa Rica, and the Colombian Andes: Constraints from global positioning system geodetic studies and gravity, in *Geologic and Tectonic Development of the Caribbean Plate Boundary in Southern Central America*, edited by P. Mann, *Spec. Pap. Geol. Soc. Am.*, *295*, 75–90.

Kent, A. J. R., E. M. Stolper, D. Francis, J. Woodhead, R. Frei, and J. Eiler (2004), Mantle heterogeneity during the formation of the North Atlantic Igneous Province: Constraints from trace element and Sr-Nd-Os-O isotope systematics of Baffin Island picrites, *Geochem. Geophys. Geosyst.*, *5*, Q11004, doi:10.1029/2004GC000743.

Klein, E. M., and C. H. Langmuir (1987), Global correlations of ocean ridge basalt chemistry with axial depth and crustal thickness, *J. Geophys. Res.*, *92*, 8089–8115.

Klein, E. M., and C. H. Langmuir (1989), Local versus global variations in ocean ridge basalt composition: A reply, *J. Geophys. Res.*, *94*, 4241–4252.

Kurz, M. D., and D. J. Geist (1999), Dynamics of the Galápagos hotspot from helium isotope geochemistry, *Geochim. Cosmochim. Acta*, *63*, 4139–4156.

Langmuir, C. H., E. M. Klein, and T. Plank (1992), Petrological systematics of mid-ocean ridge basalts: Constraints on melt generation beneath ocean ridges, in *Mantle Flow and Melt Generation at Mid-Ocean Ridges*, *Geophys. Monogr. Ser.*, vol. 71, edited by J. Phipps Morgan, D. K.

Blackman, and J. M. Sinton, pp. 183–280, AGU, Washington, D. C.

Lonsdale, P., and K. D. Klitgord (1978), Structure and tectonic history of the eastern Panama Basin, *Geol. Soc. Am. Bull.*, *89*, 981–999.

Perfit, M. R., and D. J. Fornari (1983), Geochemical studies of abyssal lavas recovered by DSRV Alvin from eastern Galápagos Rift, Inca Transform, and Ecuador Rift: 2. Phase chemistry and crystallization history, *J. Geophys. Res.*, *88*, 10,530–10,550.

Perfit, M. R., D. J. Fornari, A. Malahoff, and R. W. Embley (1983), Geochemical studies of abyssal lavas recovered by DSRV Alvin from eastern Galápagos Rift, Inca Transform, and Ecuador Rift: 3. Trace element abundances and petrogenesis, *J. Geophys. Res.*, *88*, 10,551–10,572.

Perram, L. J., and K. C. Macdonald (1994), An overlapping propagating spreading center at 87°30′W on the Galápagos Spreading Center, *Earth Planet. Sci. Lett.*, *121*, 95–211.

Plank, T., and C. H. Langmuir (1988), An evaluation of global variations in the major element chemistry of arc basalts, *Earth Planet. Sci. Lett.*, *90*, 349–370.

Saal, A. E., and J. A. Van Orman (2004), The ^{226}Ra enrichment in oceanic basalts: Evidence for melt-cumulate diffusive interaction processes within the oceanic lithosphere, *Geochem. Geophys. Geosyst.*, *5*, Q02008, doi:10.1029/2003GC000620.

Sallarès, V., and P. Charvis (2003), Crustal thickness constraints on the geodynamic evolution of the Galápagos volcanic province, *Earth. Planet. Sci. Lett.*, *214*, 545–559.

Schilling, J.-G. (1991), Fluxes and excess temperatures of mantle plumes inferred from their interaction with migrating midocean ridges, *Nature*, *352*, 397–403.

Schilling, J.-G., R. N. Anderson, and P. Vogt (1976), Rare earth, Fe and Ti variations along the Galápagos Spreading Centre and their relationship to the Galápagos mantle plume, *Nature*, *261*, 108–113.

Schilling, J.-G., R. H. Kingsley, and J. D. Devine (1982), Galápagos hotspot-spreading center system: 1. Spatial petrological and geochemical variations (83°W–101°W), *J. Geophys. Res.*, *87*, 5593–5610.

Schilling, J., D. Fontignie, J. Blichert-Toft, R. Kingsley, and U. Tomza (2003), Pb-Hf-Nd-Sr isotope variations along the Galápagos Spreading Center (101°–83°W): Constraints on the dispersal of the Galápagos mantle plume, *Geochem. Geophys. Geosyst.*, *4*(10), 8512, doi:10.1029/2002GC000495.

Shah, A. K., and J.-C. Sempéré (1998), Morphology of the transition from an axial high to a rift valley at the Southeast Indian Ridge and the relation to variations in mantle temperature, *J. Geophys Res.*, *103*, 5203–5223.

Shank, T., et al. (2003), Deep submergence synergy: *Alvin* and ABE explore the Galápagos Rift at 86°W, *Eos Trans. AGU*, *84*(41), 425, 432–433.

Sinton, C. W., D. M. Christie, and R. A. Duncan (1996), Geochronology of Galápagos seamounts, *J. Geophys. Res.*, *101*, 13,689–13,700.

Sinton, C. W., R. A. Duncan, and P. Denyer (1997), Nicoya Peninsula, Costa Rica: A single suite of Caribbean oceanic plateau magmas, *J. Geophys. Res.*, *102*, 15,507–15,520.

Sinton, J. M., D. S. Wilson, D. M. Christie, R. N. Hey, and J. R. Delaney (1983), Petrologic consequences of rift propagation on oceanic spreading ridges, *Earth Planet. Sci. Lett.*, *62*, 193–207.

Sinton, J., R. Detrick, J. P. Canales, G. Ito, and M. Behn (2003), Morphology and segmentation of the western Galápagos Spreading Center, 90.5°–98°W: Plume-ridge interaction at an intermediate spreading ridge, *Geochem. Geophys. Geosyst.*, *4*(12), 8515, doi:10.1029/2003GC000609.

Smith, W. H. F., and D. T. Sandwell (1997), Global seafloor topography from satellite altimetry and ship deep soundings, *Science*, *277*, 1956–1962.

Sours-Page, R. E., K. T. M. Johnson, R. L. Nielsen, and J. Karsten (1999), The petrogenesis of the diversity of parent magmas in the Endeavour Segment of the Juan de Fuca Ridge, *Contrib. Mineral. Petrol.*, *134*, 342–363.

Spiegelman, M., and P. B. Kelemen (2003), Extreme chemical variability as a consequence of channelized melt transport, *Geochem. Geophys. Geosyst.*, *4*(7), 1055, doi:10.1029/2002GC000336.

Sun, S.-S., and W. F. McDonough (1989), Chemical and isotopic systematics of oceanic basalts: Implications for mantle composition and processes, in *Magmatism in the Ocean Basins*, edited by A. D. Saunders and M. J. Norris, *Geol. Soc. Spec. Publ.*, *42*, 313–345.

Verma, S. P., and J.-G. Schilling (1982), Galápagos hot spot-spreading center system: 2. ^{87}Sr/^{86}Sr and large ion lithophile element variations (85°W–101°W), *J. Geophys. Res.*, *87*, 10,838–10,856.

Verma, S. P., J.-G. Schilling, and D. G. Waggoner (1983), Neodymium isotopic evidence for Galápagos hotspot-spreading centre evolution, *Nature*, *306*, 654–657.

Werner, R., K. Hoernle, U. Barckhausen, and F. Hauff (2003), Geodynamic evolution of the Galápagos hot spot system (Central East Pacific) over the past 20 m.y.: Constraints from morphology, geochemistry, and magnetic anomalies, *Geochem. Geophys. Geosyst.*, *4*(12), 1108, doi:10.1029/2003GC000576.

Wessel, P., and W. H. F. Smith (1995), New version of the Generic Mapping Tools released, *Eos Trans. AGU*, *76*, 329.

White, W. M. (1979), Pb isotope geochemistry of the Galápagos Islands, *Year Book Carnegie Inst. Washington*, *78*, 331–335.

White, W. M., and A. W. Hofmann (1978), Geochemistry of the Galápagos Islands: Implications for mantle dynamics and evolution, *Year Book Carnegie Inst. Washington*, *77*, 596–606.

White, W. M., A. R. McBirney, and R. A. Duncan (1993), Petrology and geochemistry of the Galápagos Islands: Portrait of a pathological mantle plume, *J. Geophys. Res.*, *98*, 19,533–19,563.

Wilson, D. S., and R. N. Hey (1995), History of rift propagation and magnetization intensity for the Cocos-Nazca spreading center, *J. Geophys. Res.*, *100*, 10,041–10,056.